ON THE GENERALIZATION OF SHADOWING TO FLUID TURBULENCE: PRACTICAL METHODS FOR QUANTIFYING DYNAMICAL SIMILARITY

A Dissertation
Presented to
The Academic Faculty

By

Joshua L. Pughe-Sanford

In Partial Fulfillment
of the Requirements for the Degree
Doctor of Philosophy in the
School of Physics
Center for Non-Linear Science

Georgia Institute of Technology

August 2023

ON THE GENERALIZATION OF SHADOWING TO FLUID TURBULENCE: PRACTICAL METHODS FOR QUANTIFYING DYNAMICAL SIMILARITY

Thesis committee:

Dr. Roman Grigoriev
Department of Physics
Georgia Institute of Technology

Dr. Kurt Wiesenfeld
Department of Physics
Georgia Institute of Technology

Dr. Michael Schatz
Department of Physics
Georgia Institute of Technology

Dr. Luca Dieci
Department of Mathematics
Georgia Institute of Technology

Dr. Predrag Cvitanović
Department of Physics
Georgia Institute of Technology

Date approved: June 29, 2023

It is not the world that is mysterious. Rather it is the way we view it that makes it mysterious.

George Sugihara, 2015

The voyage of discovery consists, not in seeking new landscapes, but in having new eyes.

Marcel Proust, 1923

ACKNOWLEDGMENTS

Great feats like getting a Ph.D. rarely happen in isolation. I have been so blessed over the course of my life with communities that support and uplift me, family and chosen family alike. You all mean so much to me and I couldn't have done it without you. I feel you very much with me in this moment.

I would like to thank Chris Crowley, who was the senior grad student in the Grogoriev-Schatz collaboration when I joined, and has become both an amazing friend and teacher to me. We spent many late nights writing papers together, and it didn't feel nearly as taxing as it should have, becuase he was in it with me.

I would like to give a truly special thank you to my advisor, Roman Grigoriev, who gave me so much amazing feedback during my time here, taught me to be a better scientist, and always supported me in pursuing science that excites me. I could not have asked for a better mentor.

Finally, I would like to thank the organizations that fund my group. This dissertation is based upon work supported by the National Science Foundation under Grant No. CMMI-1725587 and the Army Research Office under grant No. W911NF-15-10471. I am also deeply grateful to those that have funded me personally, including the Georgia Tech Presidential Fellowship from 2017-2021 and the Herbert P. Haley Fellowship in 2022.

TABLE OF CONTENTS

LIST OF TABLES

LIST OF FIGURES

LIST OF ACRONYMS

2D-2C two-dimensional, two-component

ECS Exact Coherent Structure

RGB red, green, and blue

RPO Relative Periodic Orbit

TCF Taylor-Couette Flow

TW Travelling Wave

SUMMARY

Chaos is an intrinsic property of many real world systems, impacting a number of today's open research questions. While many chaotic systems have known governing equations and are deterministically "solved," we still lack a comprehensive framework for predicting, controlling, and simply making sense of such systems. And while recent advances in technology allow us to explore these systems through direct numerical simulation better than ever before, the need for an insightful theoretical framework is still very much alive.

Such a framework exists in a subset of chaotic systems, known as Axiom A chaotic systems. As a result, Axiom A systems are understood quite well. However, the requirements for a system to be Axiom A are quite strict, and the overlap between systems that are Axiom A and those that are physically significant is quite small.

A very important concept in Axiom A systems is the notion of shadowing, which allows the chaotic dynamics to be decomposed piecewise-in-time in terms of much easier to analyze solutions known as periodic orbits. Periodic orbits are solutions to the governing equations that, unlike chaos, repeat in time. Their compactness make periodic orbits very simple objects to manipulate, both numerically and theoretically. This decomposition ultimately results in a predictive theory of Axiom A systems both deterministically and statistically.

In this dissertation, we seek to generalize the concept of shadowing to a broader class of (non Axiom A) chaotic systems, specifically, fluid turbulence. Although recent studies suggest that Exact Coherent Structures—e.g., repeating solutions to the Navier-Stokes equation—are descriptive of turbulence, it is an open question whether they are to turbulence what periodic orbits are to Axiom A chaos. Here, we propose a generalized method for quantifying shadowing and discuss the generalized nature of shadowing in turbulence. Our results suggest that an axiom A framework for chaos may be more generalizable than previously thought.

CHAPTER 1
INTRODUCTION

Chaotic and non-linear dynamics underpin many of the most important open questions in classical physics today. In fields like plasma physics [1], climate science [2], and even machine learning [3], chaotic dynamics are found to be pervasive. Yet, mathematicians and physicists alike are still lacking a general and effective framework for predicting and understanding such systems.

In general, what make chaotic systems so unwieldy are their characteristic sensitivity to initial conditions and their resistance to linear decomposition. The former makes chaotic systems fundamentally difficult to predict, as any uncertainty in your knowledge of the system's state will grow exponentially in time [4] and the latter renders powerful linear algebraic methods—in which dynamics are decomposed onto orthogonal subspaces of the evolution operator—useless [5]. We aim to explore an approach to chaotic dynamics that addresses both of these difficulties.

Indeed, there is light at the end of the tunnel with respect to a decomposition of chaotic dynamics, and it has been many years in the making. More specifically, there is one genre of chaotic dynamics, that of Axiom A diffeomorphisms [6, 7], that we now understand quite well through the lens of Dynamical Systems Theory.

In Dynamical Systems Theory [8], all states that can possibly describe a system are ascribed to a, potentially high dimensional, vector space known as the state space. Every point in this space is a vector $\mathbf{x} = [x_1, x_2, \dots]$ containing a list of all coordinates needed to specify a unique state of the system; in this manner, each point in the state space describes a state system the system can be in. So long as the dynamics are deterministic, the state of the system will, as it evolves, trace out a one-dimensional curve in this state space. In many chaotic systems, only a small subset of the state space, known as the chaotic

attractor, describes non-transient behavior; as such, the chaotic attractor encompasses all "characteristic" behaviors of the system.

Stated formally, a system is Axiom A if its dynamics generate a chaotic attractor, Ω, that satisfies the following properties:

A1 Ω is a compact set,

A2 Ω is everywhere hyperbolic, and

A3 periodic orbits are dense in Ω.

Letting $f^\tau(\mathbf{x}(t)) = \mathbf{x}(t+\tau)$ denote the evolution operator of the dynamics, Property **A2** enforces that there exists no $\mathbf{x} \in \Omega$ such that the Jacobian $J^t(\mathbf{x}) = \nabla_{\mathbf{x}} f^t(\mathbf{x})$ admits an eigenvalue on the unit circle for all $t \neq 0$. In turn, Property **A3** stipulates that, for every $\mathbf{x} \in \Omega$ and $\varepsilon > 0$, the ε-ball

$$B_\varepsilon(\mathbf{x}) = \{\mathbf{y} \ : \ \|\mathbf{x} - \mathbf{y}\| < \varepsilon\}$$

contains at least one periodic orbit. Periodic orbits are very special configurations of the system which, unlike chaotic trajectories, repeat in time:

$$f^{T_p}(\mathbf{x}_p(t)) = \mathbf{x}_p(t). \tag{1.1}$$

Here, T_p is the period of orbit p. We distinguish periodic trajectories, $\mathbf{x}_p(t)$, from chaotic trajectories of the system, $\mathbf{x}(t)$, via the subscript p.

Periodic orbits are very useful objects. Their compactness make them simple to store and compute properties from, and their periodicity ensures that all properties computed from them are "coordinate-free" (i.e. these properties will not depend on the choice of coordinates $x_1, x_2, \dots$) [9, Ch. 5].

Moreover, periodic orbits provide deep insight into the statistics of Axiom A systems. Indeed, Bowen [10] proved that every Axiom A system admits a Markov partition: a par-

tition of the state space in which every trajectory $\mathbf{x}(t)$ is uniquely defined by the sequence of partitions it visits. Periodic orbits represent repeating sequences and, all together, dictate which sequences are admitted by the governing equations [9, §14.6]. As a result, it is possible to show that all time-averaged statistics of Axiom A systems are computable from periodic orbits directly [9, 11]; in Axiom A chaos, there is no need to compute statistics from direct numerical simulation.

The most important property of period orbits, in the context of this work, is Property **A3**, which ensures that any point $\mathbf{x} \in \Omega$ is always infinitesimally close to some periodic state $\mathbf{x}_p$ [12]. Assuming f^τ is smooth, $\mathbf{x}(0)$ being infinitesimally close to $\mathbf{x}_p(t_0)$ guarantees that $\mathbf{x}(t)$ will evolve similar to $\mathbf{x}_p(t+t_0)$ for a finite interval of time. That is, closeness in the state space implies dynamical similarity. Specifically, if the distance between $\mathbf{x}(0)$ and $\mathbf{x}_p(t_0)$ is small, the distance between them will–on average–grow exponentially at a rate of (see [9, §21.3] and [13])

$$\|\mathbf{x}(t) - \mathbf{x}_p(t+t_0)\| \sim \left|\prod_k \Lambda_k\right|^{t/T_p} = e^{\gamma_p t}, \tag{1.2}$$

where t_0 is chosen to minimize the distance at $t=0$, $\Lambda_k = e^{\lambda_k T_p}$ are the *unstable* eigenvalues (i.e. unstable Floquet multipliers) of $J^{T_p}(\mathbf{x}_p)$ and λ_k are the corresponding Floquet exponents. A few lines of algebra give,

$$\gamma_p = \Re\left(\sum_k \lambda_k\right), \tag{1.3}$$

where $\Re$ denotes taking the real part. We refer to γ_p^{-1} as the *escape time* of orbit p; it estimates over how long the distance between $\mathbf{x}(t)$ and $\mathbf{x}_p(t)$ will remain small and for how long they will co-evolve. The chaotic trajectory is said to *shadow*[1] the periodic orbit in this interval of co-evolution. Put quantitatively, if the initial distance between the

[1]We note that here and in the turbulence literature, shadowing refers to two trajectories co-evolving. This is subtly different than the original definition, which was used to discuss whether numerically integrated trajectories approximate the exact trajectories [10, 14, 15].

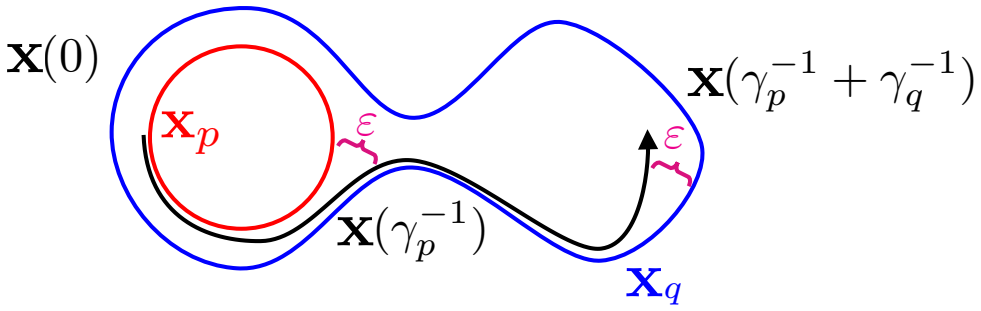

Figure 1.1: In Axiom A chaos a chaotic trajectory is always less than (magenta) away from a periodic orbit. $\mathbf{x}(t)$ (black) represents the chaotic trajectory, and $\mathbf{x}_p$ (red) and $\mathbf{x}_q$ (blue) represent periodic orbits.

chaotic trajectory and the orbit is $\varepsilon/e \ll 1$, than the evolution of the chaotic trajectory is indistinguishable—to order ε—from that of the orbit for γ_p^{-1} time units.

Shadowing, along with Property **A3**, allows for any chaotic trajectory $\mathbf{x}(t)$ in an Axiom A system to be decomposed in time as a sequence of periodic orbit sub-intervals. As illustrated in Figure 1.1, an orbit p can always be found at time $t = 0$ that is within ε/e of $\mathbf{x}(0)$. To order ε, the chaotic trajectory is well-approximated by $\mathbf{x}_p(t + t_0)$ in the interval $t \in [0, \gamma_p^{-1})$. In turn, an orbit q can then be found at time $t = \gamma_p^{-1}$ that is ε/e from $\mathbf{x}(t)$ and well-approximates $\mathbf{x}(t)$ in the interval $t \in [\gamma_p^{-1}, \gamma_p^{-1} + \gamma_q^{-1})$. And this may be continued ad infinitum. In this manner, the chaotic trajectory can be approximated to arbitrary precision as a sequence of periodic orbits.

We emphasize a few subtleties of the shadowing property:

S1 Via Equation 1.2, the derivation of the shadowing decomposition relies on the chaotic trajectory coming infinitesimally close to periodic orbits.

S2 Periodic orbits can be shadowed for intervals of time less than their period, particularly if $\gamma_p^{-1} < T_p$.

S3 There is no clear cutoff to whether the chaotic trajectory is shadowing an orbit or not; whether an orbit is considered shadowed relies entirely on the definition of ε.

S4 Property **A3** guarantees that for any orbit p that is ε away from some chaotic point

$\mathbf{x} \in \Omega$, there exists an orbit q that is $\varepsilon/2$ away from $\mathbf{x}$. There is never an orbit that is "closest" or shadowed "best." Rather, the chaotic trajectory shadows many orbits ε-well at every instant.

S5 Finally, if the chaotic trajectory shadows both orbits $\mathbf{x}_p$ and $\mathbf{x}_q$ at time t, then orbits $\mathbf{x}_p$ and $\mathbf{x}_q$ also shadow each other to order $\lesssim 2\varepsilon$ as well. Not only can the chaotic trajectory shadow orbits, but orbits may shadow each other.

Many of these subtleties are often debated in the literature of non Axiom A systems. It is important to understand the shadowing picture here, in Axiom A chaos, before moving on to more complicated dynamics.

1.1 Beyond Axiom A

Examples of Axiom A systems, such as the Bernoulli Map and Arnold's Cat Map, are usually contrived–designed to be the simplest, surmountable examples of chaos possible; chaotic systems of practical importance are rarely Axiom A. The examples mentioned above, namely plasma physics [1] and climate science [2], are not examples Axiom A chaos; they exemplify fluid turbulence. Fluid turbulence is the chaotic motion of fluids over a continuum of length and time scales, and it represents one of the most practically relevant and ubiquitous examples of chaos in existence. It is also one of the most complex examples of chaos, since it is non-linear and occurs in a very high dimensional state-space (formally an infinite dimensional state space).

In the late 1940s, Hopf conjectured that, due to dissipation, dynamics in this infinite dimensional state space will decay down onto a finite-dimensional "inertial manifold." He argued that, on this manifold, the rate of energy dissipation would on average balance the rate of energy injection into the fluid and lead to sustained dynamics while, off this manifold, only transient behavior—dominated by either dissipation or energy injection—could be observed. This inertial manifold describes a chaotic set. While this chaotic set

can be a chaotic attractor, as seen in the study of Axiom A systems, chaotic repellors are also observed in studies of turbulence [16]. Unlike for an attracting chaotic set, trajectories embedded in a repelling chaotic set will eventually exit the set as time evolves.

It has been shown that this chaotic set, as envisioned by Hopf, does not generically satisfy all of Property **A1**-Property **A3**. For instance, the chaotic repellor studied in [16] is non-compact (because it is not closed), breaking Property **A1**. That same study also found the dimension of the unstable manifold of the flow to vary across the chaotic set as well, indicating that there exists some location on the chaotic set which is not hyperbolic[2] [6], breaking Property **A2**. To date, it is not well understood whether Property **A3** is broken in turbulence.

Although fluid turbulence has been studied for quite some time, beginning with the observations of Leonardo da Vinci in the early 1500s, the notion of periodic orbits was only recently introduced to the field in the 1960s. In fact, despite the Navier-Stokes equations—the deterministic equations governing the evolution of fluids—being derived by the 1850s, early approaches to turbulence were largely statistical, including Kolmogorov's scaling law [17] and the law of the wall [18]. These theories, which leveraged dimensional analysis and the assumption of spatial uniformity and/or isotropy, were reasonably successful, but were not directly related to the Navier-Stokes equations. Moreover, while these theories excelled in describing isotropic turbulence, they proved inadequate in capturing the fleeting patterns and spatiotemporal correlations that many real-world turbulent flows exhibit.

While this claim was never published, it is Hopf who is credited with originally conceptualizing turbulence as a meandering walk between these fleeting, unstable flow patterns [9, section A1.5]. This perspective, which incorporated the rich correlated structures of turbulence, offered a new way to investigate fluid motion. Long-established observations [19] of these flow patterns not only made concrete their importance to turbulence, but earned them the name *coherent structures* by the fluid mechanical community. Around the same

[2] An eigenvalue of J^t must cross the unit circle on the boundary at which the dimension of the unstable manifold changes.

time, Smale [20] and Anasov [14] where highlighting the importance of periodic orbits in Axiom A chaos. Speigel and Moore began to advocate a description of turbulence in terms of unstable periodic solutions [21, 22] and Christiansen et al. [23] were the first to apply this description to a spatially extended system, the Kuramoto-Sivashinsky equation, in the late 1990s. As technology improved, the advent of advanced numerical methods such as Newton-Krylov solvers [24] enabled the computation of such unstable periodic solutions in turbulence as well. Unlike coherent structures, which are fleeting, these solutions repeat in time *exactly* and, like coherent structures, these solutions can exhibit spatial [25] and temporal [26] features qualitatively similar to those of turbulence. As a result, these solutions become known as Exact Coherent Structures (ECSs) by the fluid mechanical community.

While it is unclear whether ECSs are generically dense in turbulence, it is proven that periodic orbits can be dense in sub-regions of the turbulent chaotic set. In 1899, Poincaré proved that when there exists a periodic orbit admitting a homoclinic connection—a non-chaotic trajectory that describes destabilization off of and subsequently re-stabilization back on to the base orbit—then there exists in a dense set of other periodic orbits in the neighborhood of that base orbit [27]. These dense neighborhoods, known as homoclinic tangles, have recently been observed in turbulent edges states [28] and turbulence itself [29], providing concrete evidence that periodic orbits can be dense within subsets of the chaotic set of turbulence. Property **A3**, however, is nevertheless unproven. To complicate matters further, ECSs encompass a much broader class of recurrent solutions than just periodic orbits and it is unclear how these various kinds of ECSs pertain to Property **A3**.

The simplest types of ECSs that occur in turbulence are equilibria [30, 31, 32, 33, 34] and, in systems possessing a continuous spatial symmetry, Travelling Waves (TWs) [31, 35, 36, 37, 38, 39, 40, 41, 42], which are equilibria in suitable co-moving reference frames. Much of the prior work exploring the role of ECSs in turbulence focused on TWs [35, 42], rather than periodic orbits. There is experimental evidence of the role of TWs in the transition from laminar flow to turbulence [36, 37, 38] and TWs were even found to

be visited by turbulent flow in numerical simulations of channel flow [39] and pipe flow [41, 40]. However, TWs are too simple to describe the rich temporal dynamics of fluid turbulence. Recent work has established that ECSs with nontrivial temporal behavior, like periodic orbits and their higher order analogs, are better suited for this purpose [26, 43].

Periodic orbits [26, 43] represent the simplest ECSs that have non-trivial time dependence and, as previously indicated, have been found to characterize turbulence, in two-dimensional [44], quasi-two-dimensional [45] and three-dimensional [43] flows alike. In systems with a continuous symmetry, such as pipe flow, Relative Periodic Orbits (RPOs) are infinitely more likely to exist than periodic orbits. Much like TWs represent equilibria in a suitably chosen co-moving reference frame, RPOs represent periodic orbits in a suitably chosen co-moving reference frame. ECSs of even greater complexity, such as 3-tori [46], exist in turbulence as well.

Much of the previous work suggested the relevance of ECSs to turbulence via finding instances of visual similarity between snapshots of the ECS flow field with that of turbulent flow as. For instance, Hof *et al.* [36]'s seminal work in pipe flow uncovered the visual similarity between turbulence and travelling waves. Visual similarity is synonymous with the instantaneous state space distance between a turbulent state and the ECS being *somewhat* small. Hence, as technology progressed, many searched for "close passes"—moments in which the instantaneous state space distance between turbulence and ECSs is small relative to its mean—to indicate the dynamical relevance of ECSs. As we shall see in Chapter 2, state space distances during a "close pass" are not ε-small. This usage of the term "close" in the turbulence literature is markedly different from the use of *infinitesimal* closeness in the Axiom A literature. From an Axiom A perspective, it is infinitesimal closeness that guarantees shadowing, not the "closeness" implied by visual similarity.

Other studies use the qualitative similarity of *trajectories* in the state space as an indicator of dynamical similarity between ECSs and turbulent flow [47, 43]. Because this measure incorporates temporal information about the evolution of the turbulent and ECS tra-

jectories, it is a better indication of shadowing. However, it is still largely qualitative, often incorporating low-dimensional linear projections [47] or temporal averaging [43] that can be misleading. Although lacking quantification, these previous qualitative results heavily suggest that shadowing occurs in turbulence, despite the lack of Property **A1**-Property **A3**.

Further indications of the importance of ECSs include that, much like periodic orbits in Axiom A chaos, collections of ECSs can reproduce certain statistical properties of weakly turbulent flow. Even a single time-periodic solution obtained by Kawahara and Kida [43] for plane Couette flow was found to reproduce, with fairly high accuracy, both the mean flow profile and the fluctuations in all three components of the velocity. Moreover, a Markov model constructed from ECSs was found produce the statistics of turbulence quite well [48]. Intriguingly, this Markov model is different than the one discussed by Bowen [10]; recent studies [29, 48, 49, 9, 50, 51] have opted to use the disjoint neighborhoods of ECSs as partitions and compute the transition probabilities empirically. Markov models seem to be effective for many choices of partitions [52, 53] and it is unclear whether the distinction between this choice of partition and Bowens' is important. In any case, the statistics of turbulent flow appear to be computable from ECSs [48, 54, 55].

It is therefore natural to ask whether these results are coincidental or whether collection of ECSs can be for fluid turbulence what periodic orbits are to Axiom A chaos. We aim to answer this question in the following dissertation and, most importantly, compare the observed nature of shadowing in turbulence to the properties listed in Property **S1**-Property **S5**.

The remainder of this dissertation is structured as follows: Chapter 2 introduces Taylor-Couette flow, the system in which we will study fluid turbulence and shadowing. Chapter 3 presents two quantitative measures of shadowing in turbulence and summarizes the work published in [16, 56, 57] that applies these methods in Taylor-Couette flow. Chapter 4 presents a summary of our understanding of shadowing in turbulence at this point in time and discusses avenues for future work.

CHAPTER 2

TAYLOR-COUETTE FLOW

Although highly promising, existing evidence of the role of ECSs in turbulent flows is largely circumstantial and comes primarily from idealized numerical simulations. In particular, it remains unclear whether realized (that is, experimental) three-dimensional turbulent flows shadow any ECSs. Often, experimental data (acquired in large and/or open spatial domains) is difficult to compare with simulation (computed in minimal flow units or in highly symmetric sub-spaces of the state space or with unphysical—e.g. periodic—boundary conditions). In order to conclusively answer this question, ECSs must be computed on a domain and with boundary conditions realizable in experiment. This disparity can be resolved by studying a closed flow, where the boundary conditions in the flow direction are naturally periodic and laboratory observations can be directly compared with ECSs. For this reason, we study the RPO between two concentric, independently rotating cylinders.

Taylor-Couette Flow (TCF) is governed by the Navier-Stokes equation along with an incompressibility condition. Both may be written in non-dimensional form using the gap width w and the diffusive time scale w^2/ν as the length and time scale, respectively:

$$\begin{aligned} \partial_t \mathbf{u} + (\mathbf{u}\cdot\nabla)\mathbf{u} &= -\nabla P + \nabla^2 \mathbf{u}, \\ \nabla\cdot\mathbf{u} &= 0. \end{aligned} \tag{2.1}$$

Here, $\mathbf{u} = (u_r, u_\theta, u_z)$ and P are the non-dimensional velocity and pressure. The dynamics are parametrized by five non-dimensional parameters. Two of these are geometrical:

$$\Gamma = h/w \qquad\qquad \eta = r_i/r_o,$$

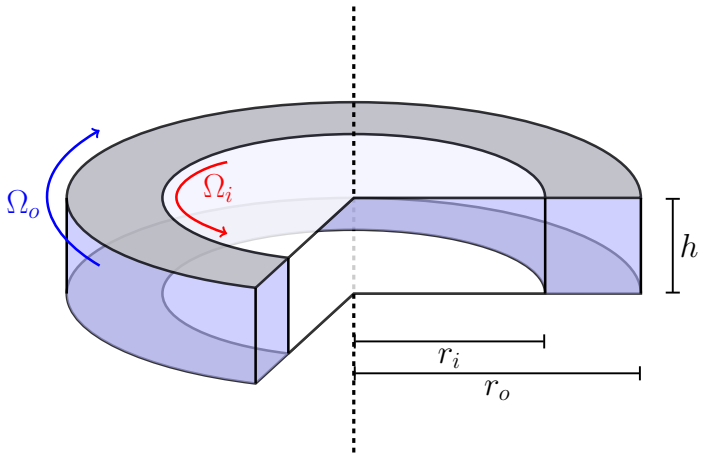

(a)

Figure 2.1: Geometry of the Taylor-Couette flow driven by counter-rotating cylinders. The fluid domain is shaded purple.

where h is the height of the fluid layer, $w = r_o - r_i$ is the gap width between the cylinders, and r_i and r_o are the radii of the inner and outer cylinder, respectively, as shown in Figure 2.1. The remaining three parameters are Reynolds numbers describe how the system is forced at the boundary:

$$Re_i = \Omega_i r_i w/\nu \qquad Re_o = \Omega_o r_o w/\nu \qquad Re_e = \Omega_e r_o w/\nu,$$

where ν is the kinematic viscosity of the fluid, Ω_i and Ω_o are the angular velocities of the inner and outer cylinders, respectively, and Ω_e is the angular velocity of the top and bottom end-caps . No-slip boundary conditions are imposed on all the walls such that

$$\begin{aligned} \mathbf{u}(r_i, \theta, z, t) &= (0, Re_i, 0), \\ \mathbf{u}(r_o, \theta, z, t) &= (0, Re_o, 0), \\ \mathbf{u}(r, \theta, \pm h/2, t) &= (0, Re_e\ r/r_o, 0). \end{aligned} \tag{2.2}$$

The last relation describes the boundary conditions at the top and bottom of the fluid layer. Two distinct sets of boundary conditions are investigated in this dissertation.

TCF(a) will refer to $(Re_i, Re_e, Re_o) = (1200, 0, -1200)$ at aspect ratio $\Gamma = 1$ and radius ratio $\eta = .50$, and TCF(b) will refer to $(Re_i, Re_e, Re_o) = (500, -200, -200)$ at aspect ratio $\Gamma = 1$ and radius ratio $\eta = .71$. Both are flows driven by counter-rotating cylinders and in the wide-gap, small-aspect-ratio parameter regime. Notice that in the former, the top and bottom end caps are chosen to be stationary ($Re_e = 0$), and in the latter they co-rotate with the outer cylinder ($Re_e = Re_o$). Both configurations were investigated numerically by Krygier [58] in his thesis. An experimental realization of TCF(b) was constructed by Crowley [59].

2.1 Numerical Methods

Direct numerical simulations (DNS) of all TCFs were performed using a pseudo-spectral code [60, 61, 62, 58] which solves the governing equations in cylindrical coordinates (r, θ, z). The velocity field $\mathbf{u}$ at location (r, θ, z) and time t is given by

$$\mathbf{u}(r, \theta, z, t) = \Re \sum_{k=0}^{N_r} \sum_{l=0}^{N_z} \sum_{m=0}^{N_\theta/2} \mathbf{U}^{klm}(t) T_k(\rho) T_l(\zeta) e^{im\theta}, \tag{2.3}$$

where $\rho = (2r - r_i - r_o)/d$ and $\zeta = 2z/h$. N_r, N_z, and N_θ are the number of spectral modes in the three coordinate directions, $T_k(\cdot)$ is the Chebyshev polynomial of order k, and $\Re$ denotes the real part. The solution is advanced in time using a second order stiffly stable time-splitting scheme [63]. Advection terms are evaluated on the spatial grid (r_k, z_l, θ_m) in physical space, where

$$\begin{aligned} r_k &= \frac{(r_o - r_i)\cos(k\pi/N_r) + r_i + r_o}{2}, & k &= 0, \ldots, N_r, \\ z_l &= \frac{\Gamma \cos(l\pi/N_z)}{2}, & l &= 0, \ldots, N_z \end{aligned} \tag{2.4}$$

are Chebyshev collocation points and $\theta_m = 2\pi m/N_\theta$ with $m = 0, \ldots, N_\theta - 1$. The Helmholtz and Poisson equations are solved efficiently using a complete diagonalization

of the operators in both the radial and axial direction for each Fourier mode [64].

We set $N_r = 32$, $N_\theta = 128$, $N_z = 48$ (i.e., corresponding to a $3(N_r+1)(N_z+1)N_\theta = 620,928$ dimensional state space) and select a time step that accurately resolves the spatial structure and temporal dependence of all computed flow fields. The spatial resolution was chosen such that the magnitude of the spectral coefficients $\mathbf{U}^{klm}$ decreases by at least four orders of magnitude for ECSs (and at least three orders of magnitude for turbulent flows) as k, l, or m increases from the smallest to the largest value.

2.2 Computation of Exact Coherent Structures

Under the boundary conditions described by Equation 2.1, TCF is invariant under arbitrary rotations R_ϕ about the z-axis and reflections K_z about the mid-plane $z = 0$, where

$$R_\phi \mathbf{u}(r,\theta,z,t) = \mathbf{u}(r,\theta+\phi,z,t), \tag{2.5}$$

$$K_z \mathbf{u}(r,\theta,z,t) = (u_r, u_\theta, -u_z)(r,\theta,-z,t). \tag{2.6}$$

These transformations form a symmetry group $\mathcal{G} = \mathrm{SO}(2) \times \mathrm{Z}_2$. The presence of continuous rotational symmetry and the lack of reflection symmetry in θ imply that the dynamically relevant ECSs in Taylor-Couette flow are relative, for example, RPOs and TWs. In particular, RPOs satisfy

$$\mathbf{u}(T) - R_\Phi \mathbf{u}(0) = \mathbf{0}, \tag{2.7}$$

where Φ and T are the solution's rotational shift and period, respectively. The angular velocity of this co-rotating reference frame is $\Omega = \Phi/T$. TWs also satisfy Equation 2.7 for $T = \Phi/\Omega$ at arbitrary Φ. While relative pre-periodic orbits may also exist due to the K_z symmetry, we do not need to search for them explicitly; any pre-periodic orbit will also satisfy Equation 2.7 over two periods. Indeed, Equation 2.7 serves as a catch-all equation

Table 2.1: Properties of ECSs found in TCF(a): the temporal period T and shift Φ. The dimension of the unstable manifold of each solution, N^u is also shown, as well as the escape time, γ^{-1}. Both the period and escape time are in non-dimensional time units. N^u includes the two (one) marginally stable directions of each RPO (TW) along τ and ϕ. The discrete spatial symmetries of solutions are listed, if they possess any.

$\mathbf{u}_n$	T	Φ	N^u	γ^{-1}	Discrete Symmetry
TW_{01}	0.1305	π	11	0.0121	$K_z R_{\pi/2}$
TW_{02}	0.0127	π	11	0.0026	R_π
TW_{03}	0.0459	2π	44	0.0004	$K_z R_\pi$
RPO_{01}	0.0159	0.3541	6	0.0228	$K_z R_{\pi/2}$
RPO_{02}	0.0501	0.8275	11	0.0063	
RPO_{03}	0.0506	0.8817	6	0.0095	
RPO_{04}	0.0512	0.9676	7	0.0205	
RPO_{05}	0.0262	3.4118	7	0.0227	
RPO_{06}	0.0063	3.2688	8	0.0247	
RPO_{07}	0.0213	0.1581	6	0.0210	R_π
RPO_{08}	0.0493	0.9091	10	0.0124	
RPO_{09}	0.0191	3.4949	5	0.0214	
RPO_{10}	0.0194	3.4615	6	0.0152	
RPO_{11}	0.0196	3.4271	7	0.0159	
RPO_{12}	0.0217	0.1442	7	0.0193	R_π
RPO_{13}	0.0081	1.1617	11	0.0051	R_π
RPO_{14}	0.0446	5.0016	11	0.0077	
RPO_{15}	0.0073	1.3298	12	0.0045	R_π
RPO_{16}	0.0063	1.6429	12	0.0039	
RPO_{17}	0.0121	0.3186	17	0.0016	R_π
RPO_{18}	0.0558	2.2912	9	0.0084	
RPO_{19}	0.0451	0.7489	14	0.0021	
RPO_{20}	0.0361	3.9396	11	0.0084	

for the solutions expected to exist in TCF. For solutions with an N-fold discrete rotational symmetry, we arbitrarily restrict $0 \leq \Phi < 2\pi/N$ to make the definition of rotational shift unique.

Solutions of Equation 2.7 are found using an in-house Newton-GMRES solver [58] that leverages a hookstep algorithm [24]. Since Newton's method is not globally convergent, sufficiently good initial guesses had to be supplied to this solver. To accomplish this, deep

Table 2.2: Properties of RPOs found in TCF(b): the temporal period T and shift Φ. The dimension of the unstable manifold of each solution, N^u is also shown, as well as the escape time, γ^{-1}. Both the period and escape time are in non-dimensional time units. N^u includes the 2 marginally stable directions of each solution, along τ and ϕ. None of the above solutions possess discrete spatial symmetry.

$\mathbf{u}_n$	T	Φ	N^u	γ^{-1}
RPO_1	0.196	1.043	9	0.0246
RPO_2	0.177	0.856	7	0.0209
RPO_3	0.234	0.448	9	0.0260
RPO_4	0.200	0.199	8	0.0299
RPO_5	0.422	0.443	7	0.0336
RPO_6	0.419	0.425	8	0.0358
RPO_7	0.164	0.481	8	0.0342
RPO_8	0.215	5.799	8	0.0464

minima of the recurrence function [26],

$$G(t,\tau) = \min_{\phi} \|\mathbf{u}(t+\tau) - R_\phi \mathbf{u}(t)\| \tag{2.8}$$

were tabulated, which correspond to instances in which a turbulent trajectory $\mathbf{u}(t)$ is almost periodic or stationary in the co-moving frame. Details of how these trajectories were initialized and computed are provided in [58]. Distance is computed with respect to the L_2 norm

$$\|\mathbf{f}\| = \left(\int_V f_r^2(r,\theta,z) + f_\theta^2(r,\theta,z) + f_z^2(r,\theta,z)\, dV \right)^{\frac{1}{2}} \tag{2.9}$$

over the entire volume V of the flow domain. Some of these minima correspond to close passes to RPOs or TWs, and the corresponding flow fields $\mathbf{u}(t)$, time delays τ, and rotation angles ϕ represent good initial conditions for the solver.

Once solutions are found, they may be numerically continued in Re_i using pseudo-arclength continuation [65]; some branches turn around, yielding several additional solutions. All solutions used in this study are listed in Table 2.1 and Table 2.2. Notably, no pre-periodic solutions were found in either system. For more detail on TCF(a), we point

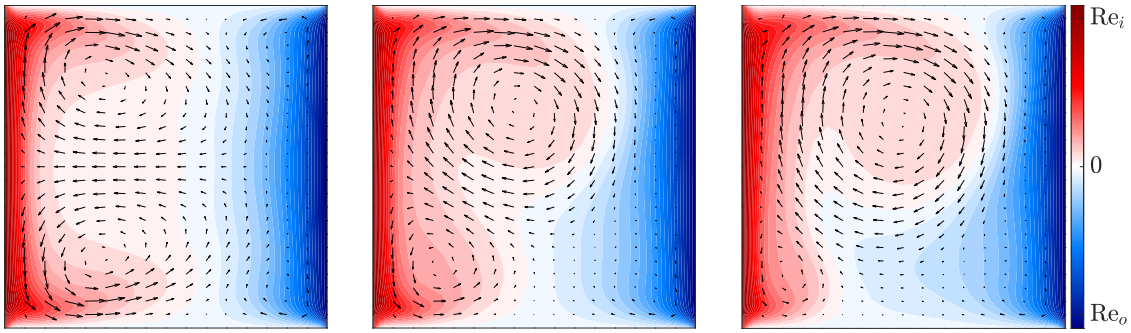

Figure 2.2: Mean flow profile of TCF(a) in (a) lobe 1, (b) lobe 2, and (c) lobe 3. Arrows show the in-plane (r and z) components of the flow and the color indicates the out-of-plane (θ) component.

the reader to [58]. Similarly, for more detail on TCF(b), we point the reader to [16, 56, 57].

2.3 Dynamics of TCF(a)

Described best by Krygier *et al.* [16], characterizing the chaotic set of TCF(a) was an involved yet illuminating process. For example, a collection of ECSs were found to be grouped away from the turbulence trajectory and they were used to infer the existence of (and compute) an entirely unexplored region of the chaotic set. We will give only an abridged discussion of the chaotic set here.

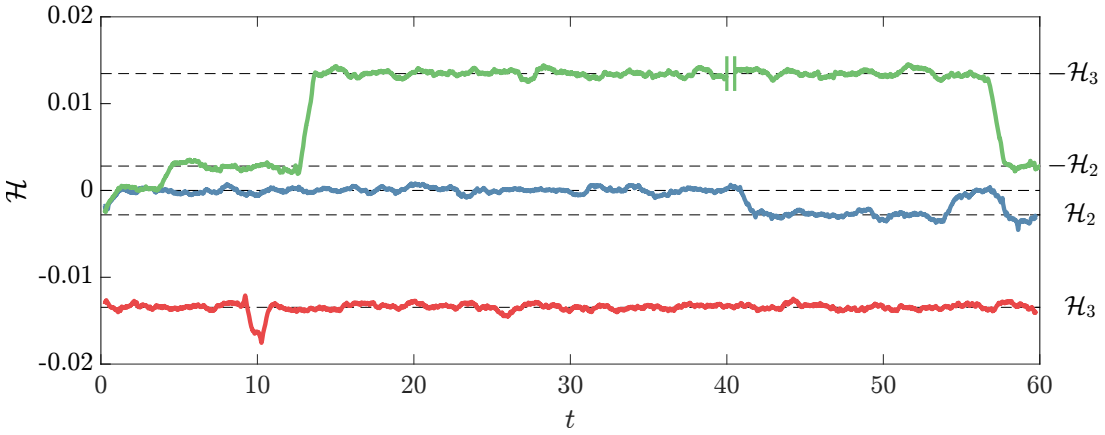

Figure 2.3: Helicity over three simulated turbulent trajectories of TCF(a). Shown is the running average taken over a window of 1 time unit. Note that 10 time units are removed from green trajectory at $t = 40$, during which the flow remains in lobe 3. The mean helicity of each lobe are illustrated with black dashed lines.

As demonstrated by [16], the chaotic set of TCF(a) is characterized by five distinct but dynamically connected regions in the state space, referred to as "lobes" of the chaotic set. The characteristic flow fields in each lobes are compared in Figure 2.2, where the velocity field associated with each region has been averaged in both time and θ. Inside each lobe, we find two cellular vortical structures. In lobe 1, the two vortices are symmetric and hence lobe 1 is symmetric under the action of K_z. In lobes 2 and 3, one vortex is notably stronger than the other and, as a result, there are two other lobes that correspond to the image of lobes 2 and 3 under the action of K_z. The normalized helicity,

$$\mathcal{H} = \frac{1}{Re^2 V} \int_V \mathbf{u} \cdot \boldsymbol{\omega} \, dV. \tag{2.10}$$

is invariant under R_ϕ but changes sign under K_z. Here $Re = |Re_i - Re_o|/2$ is the characteristic scale for the velocity and $\boldsymbol{\omega} = \nabla \times \mathbf{u}$ is the vorticity. As demonstrated by Figure 2.3, which plots $\mathcal{H}$ over three different simulations of turbulence, each lobe presents with a characteristic value of helicity; the degree of z-asymmetry in each lobe explains the relative arrangement of the three lobes along the $\mathcal{H}$ axis. Figure 2.3 illustrates that turbulence hops between all lobes and that all lobes are (bidirectionally) dynamically connected.

Eventually, turbulent flow escapes the chaotic set composed of the five lobes (not shown) and settles on what appears to be a stable quasi-periodic state. Hence, the dynamics of TCF(a) describe a long-lived transient, similar to what was found at an identical radius ratio but larger aspect ratio [66].

Our library of ECSs appear to be collocated with two out of the three lobes. While it is impossible to visualize the infinite-dimensional state space, low-dimensional projections can provide insight. Given the continuous symmetry of TCF, it is easiest to understand the state space geometry in coordinates (observables) that are invariant under rotation. The normalized energy

$$\mathcal{E} = \frac{1}{Re^2 V} \int_V \mathbf{u}^2 \, dV, \tag{2.11}$$

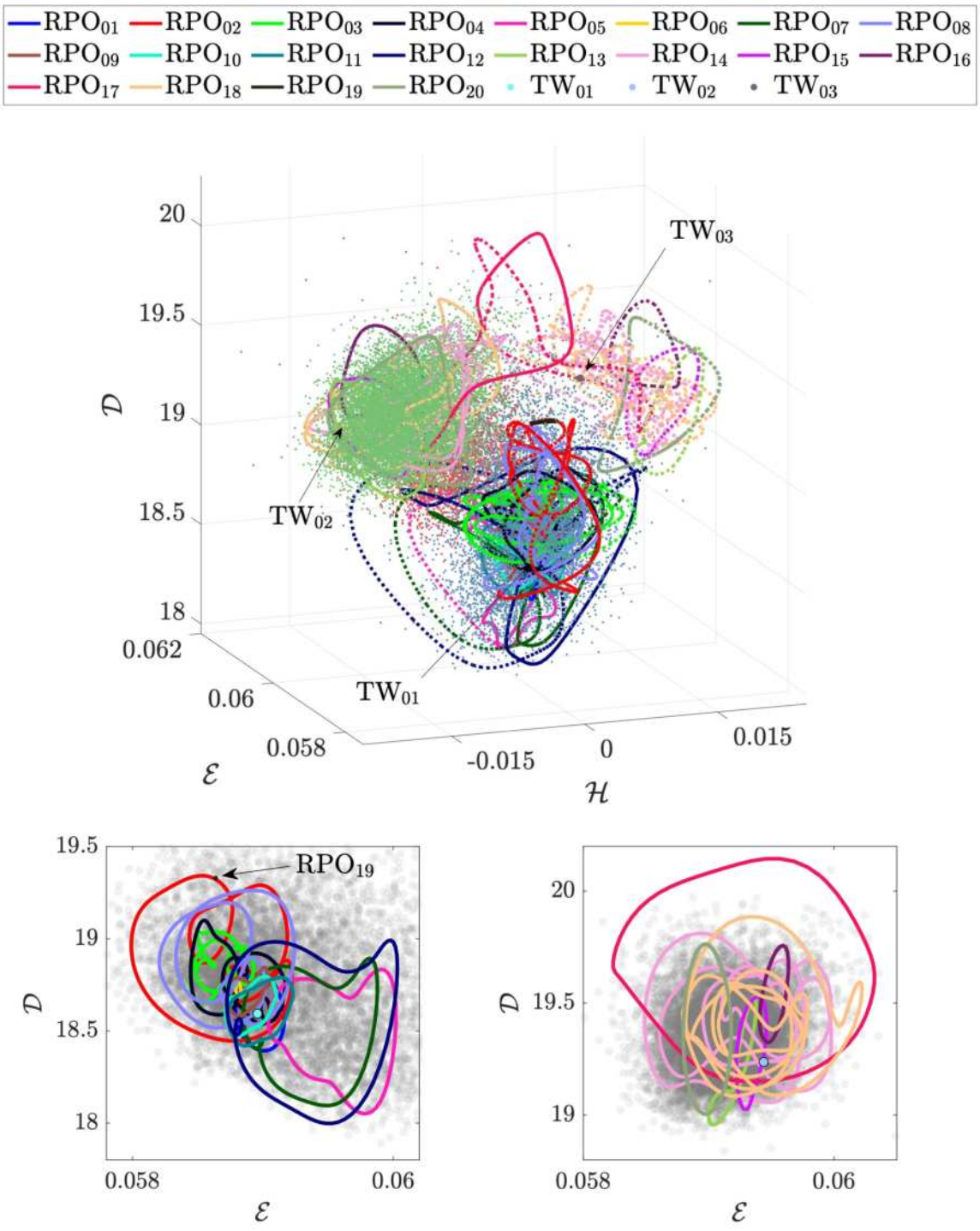

Figure 2.4: (top) Three-dimensional projection of the infinite-dimensional state space. The coordinates used are the energy $\mathcal{E}$, the rate of energy dissipation $\mathcal{D}$, and the helicity $\mathcal{H}$. The individual lobes of TCF(a)'s chaotic set are shown as clouds of points with different color; lobe 1 shown in blue, lobe 2 in red, and lobe 3 in green. (bottom) Close up, two-dimensional projections in lobes 1 (bottom left) and 3 (bottom right). The chaotic set (gray) is in the background and RPOs and TWs collocated with each lobe in this projection are overlaid as solid curves and filled circles, respectively.

and rate of energy dissipation

$$\mathcal{D} = \frac{1}{Re^2 V} \int_V \boldsymbol{\omega}^2 \, dV, \tag{2.12}$$

in addition to helicity, provide us three rotationally invariant coordinates with which to plot a projection in the state space, see Figure 2.4. Intervals of turbulence confined to lobes 1, 2, and 3 are plotted as blue, red, and green point clouds, respectively. Each dot represents a snapshot of the flow. For each ECS $\mathbf{u}_n$ that is not reflection-symmetric, both $\mathbf{u}_n$ (solid) and $K_z\mathbf{u}_n$ (dashed) are shown as colored curves. Since all three coordinates are invariant with respect to rotations around the axis, the family of temporally periodic solutions corresponding to each TW (i.e., $R_\phi \mathbf{u}_n$ with $\phi \in [0, 2\pi)$) is mapped to a single point. Similarly, the family of temporally quasi-periodic solutions corresponding to each RPO is mapped to a single closed curve. As mentioned previously, a large number of computed ECSs appear to be collocated with lobes 1 and 3. Although initial guesses sampled from lobe 2 were fed into the Newton-Krylov solver, all searches initialized in this region stagnated or converged to solutions outside of lobe 2. No solutions are found to be collocated with lobe 2 in projection.

To compare the temporal structure of turbulence with our library of ECSs, consider a projection onto the tuple

$$\mathbf{c}(t, \theta) = \frac{1}{hw} \int dr dz \, (u_r, u_z, u_\theta) \tag{2.13}$$

Normalizing each component of $\mathbf{c}$ to take on a value between 0 and 1, this tuple may be considered a red, green, and blue (RGB) triplet—a color. While this RGB-projection retains very little quantitative information, it illustrates spatio-temporal patterns in the flow quite well, see Figure 2.5. The spatio-temporal features of turbulence change drastically between lobes 1, 2 and 3. Despite turbulence never coming infinitesimally close to known ECS, these RGB plots suggest that certain ECSs (TW_{01}, RPO_{01}-RPO_{12}, and RPO_{19}) appear

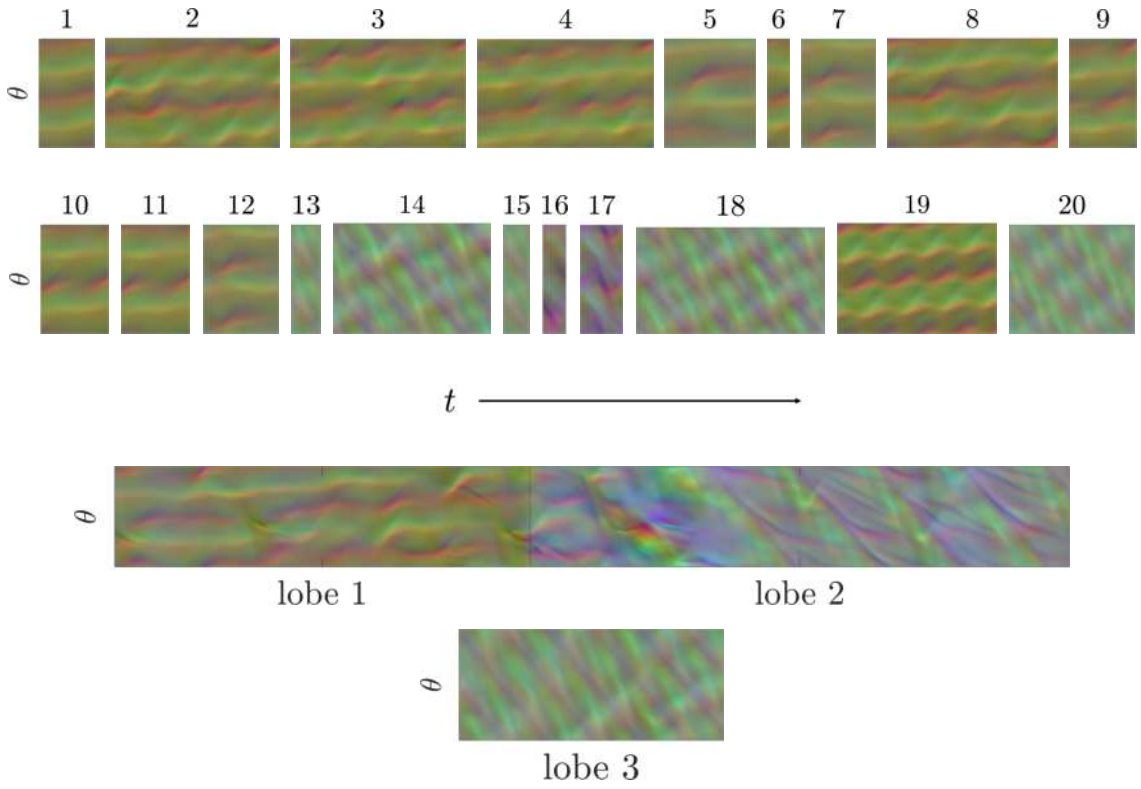

Figure 2.5: An RGB plot (Equation 2.13) of each RPO over one period and an representative interval of turbulence in each lobe. Time evolves from left to right in all plots. Each RPO is labeled by its index n and shown in its own co-moving reference frame, such that the fields are periodic in both space and time. Turbulence is plotted in the lab frame. The dashed line denotes where turbulence begins to transition between lobes 1 and 2.

to be descriptive of the spatial *and* temporal dynamics of lobe 1, while other ECSs (RPO_{13}-RPO_{14}, RPO_{18}, and RPO_{20}) appear to do the same for lobe 3.

Figure 2.5 also suggests that certain groupings of RPOs—for example RPOs 2 and 8; RPOs 3 and 4; RPOs 9, 10, and 11; and RPOs 7 and 12—are related. As discussed in [16], each of these groups correspond to RPOs that are connected through bifurcations.

Finally, Figure 2.5 suggests that RPO_{19} is period-4 solution from a series of period doubling bifurcations off of some fundamental RPO. This is also indeed the case, and other solutions in this series were computed since the publication of [16].

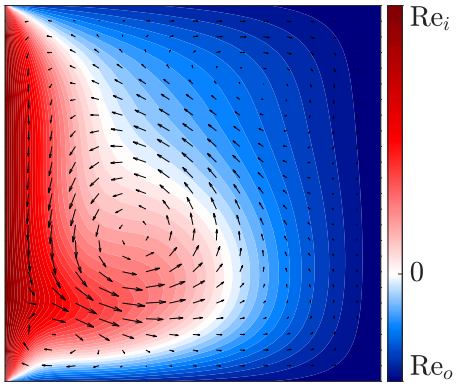

Figure 2.6: Mean flow profile of TCF(b). Arrows show the in-plane (r and z) components of the time-averaged flow and the color indicates the out-of-plane (θ) component.

2.4 Dynamics of TCF(b)

The chaotic set is much simpler to describe in this geometry, see Figure 2.7. Over 60 non-dimensional time units of turbulent flow, only one fundamental lobe is observed. The mean flow profile of this lobe is plotted in Figure 2.6. Similar to lobes 2 and 3 in TCF(a), this lobe is K_z-asymmetric, ensuring the existence of a symmetry related copy. However, unlike in TCF(a), no transitions are observed between lobes. In other words, K_z symmetry is spontaneously broken in TCF(b).

TCF(b) may also be viewed in the $\mathcal{EDH}$-projection. In projection, all ECSs in our library appear to be collocated with the chaotic set, as illustrated in Figure 2.7(a,b). The dynamics of TCF(b) appear to be dominated by a large scale oscillation of with a period of about $\sim .235$ time units, as illustrated in Figure 2.7(c); the chaotic nature of the dynamics are expressed, then, as the perturbation to this time-periodic base flow. This suggests that the dynamics of TCF(b) may admit a Poincaré plane which quotients this base, cyclic component of the dynamics. However, the existence of such a Poincaré plane will not be explored here.

In an RGB projection, Figure 2.8, a red-green structure is observed approximately every $\sim .235$ time units, as the system excurs into the high-dissipation region of the chaotic set. Two ECSs, RPOs 5 and 6, have periods about twice that of the other solutions. Indeed, as

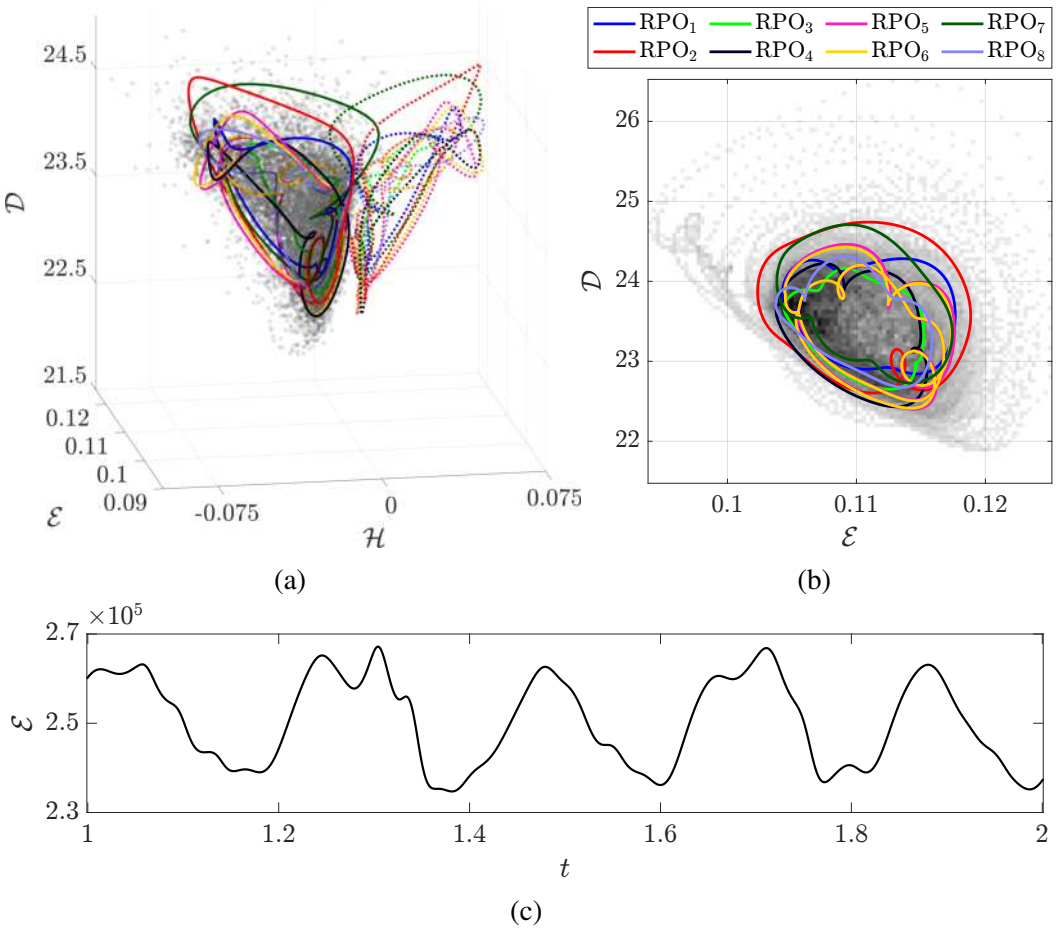

Figure 2.7: Three-dimensional projection of the infinite-dimensional state space (left) and a corresponding two-dimensional projection (right). The coordinates used are the energy $\mathcal{E}$, the rate of energy dissipation $\mathcal{D}$, and the helicity $\mathcal{H}$. The computed RPOs are shown as solid lines and their symmetry-related copies as dotted lines of the same color. The chaotic set is shown as a cloud of transparent grey points in the 3D projection and as a histogram in the 2D projection (darker regions have higher likelihood of visitation). (c) $\mathcal{E}$ is plotted for a small interval of the turbulent trajectory for $t \in [1, 2]$, illustrating its qualitatively periodic nature.

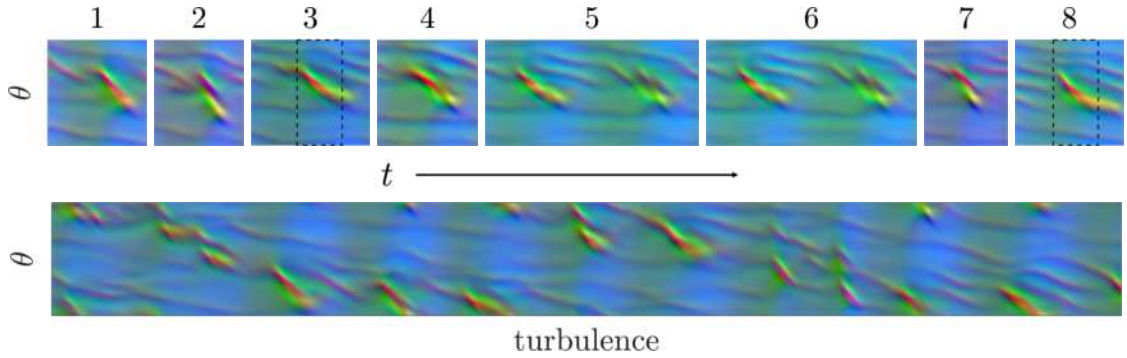

Figure 2.8: An RGB plot (Equation 2.13) of each RPO over one period and an representative interval of turbulence in each lobe. Time evolves from left to right in all plots. All fields are plotted in the lab frame, such that RPO may not appear periodic in time. The sub-intervals of RPO 3 and 8 that are bolded in Figure 3.13(b) are indicated with a dashed black line.

visible in Figure 2.8, RPO 5 and 6 seems to make two excursions (two red-green structures are observed) into the high dissipation regime every period, while the other solutions excur only once (one red-green structure is observed). Moreover, this projection emphasizes that RPO 5 and 6 are related, nearly identical. As discussed by Crowley *et al.* [56], RPO 5 and 6 are related via a nearby bifurcation at $Re_i = 500.39$.

2.5 Closeness in the State Space

In low-dimensional systems, the discussion of shadowing is founded upon the chaotic system always being infinitesimally close to an invariant set (Property **S1**). In higher dimensions, distances tend to be larger [67, §2.5], an effect coined "the curse of dimensionality." In Axiom A chaos, this scaling is unimportant since periodic orbits are dense. However, in turbulence, this poses are real problem.

The degree of closeness between turbulence and ECSs is simple to investigate via direct inspection. We may define the distance from an arbitrary trajectory $\mathbf{u}(t)$ in the state space to an ECS to be

$$d_n^{\perp}(t) = \min_{\phi,\tau} \|\mathbf{u}(t) - R_\phi \mathbf{u}_n(\tau)\|, \tag{2.14}$$

minimizing over all possible rotations R_ϕ and temporal snapshots of the ECS. Here, $\tau \in [0, T_n)$ defines the temporal phase along solution $\mathbf{u}_n$ ($\tau = 0$ for TWs since time evolution is equivalent to rotation). Notice that since no pre-periodic solutions were discovered, there is no need to minimize distances over the K_z symmetry.

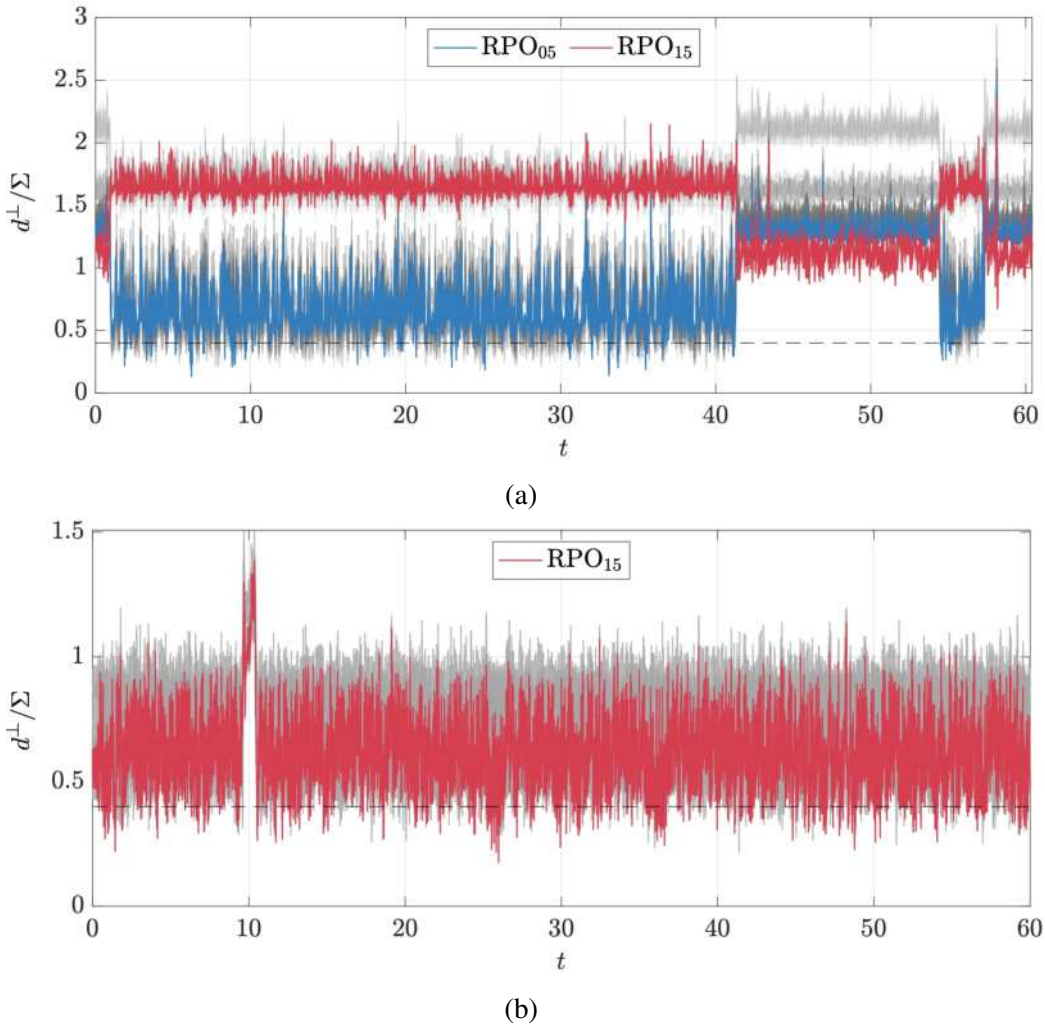

Figure 2.9: The normalized distance $d^\perp/\Sigma$ is plotted for every ECS $\mathbf{u}_n$ in TCF(a) over numerical trajectories that explore (a) lobes 1 and 2 and (b) lobe 3 of the chaotic set. All ECSs except for RPO_{05} (blue) and RPO_{15} (red) are shown in gray. The dashed line indicates the threshold, $D_{\text{vis}} = .4$, below which flow fields appear visually similar, see Figure 2.11.

A choice of distance scale for any set $\mathcal{R}$ in the state space is given by

$$\Sigma = \langle \|\mathbf{u} - \langle \mathbf{u} \rangle_{\mathcal{R}}\| \rangle_{\mathcal{R}}, \tag{2.15}$$

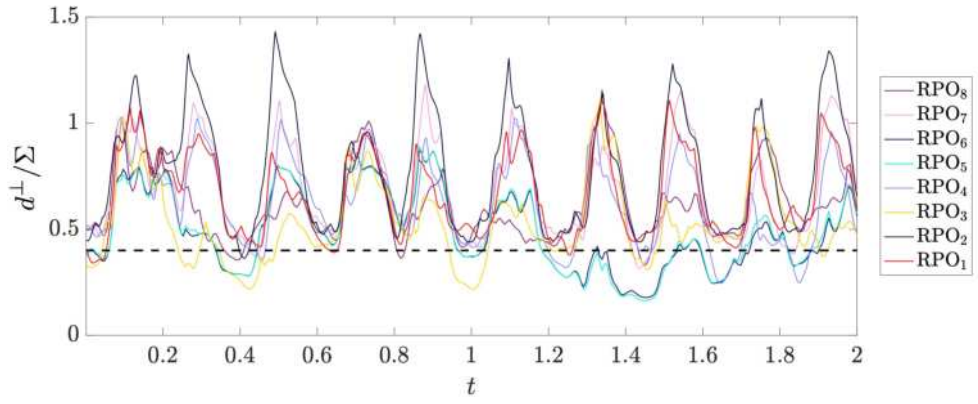

Figure 2.10: The normalized distance $d^\perp/\Sigma$ is plotted for every ECS $\mathbf{u}_n$ in TCF(b) over a representative interval of turbulent data. While the full data set spans $t \in [0, 60]$, only a portion of that interval is shown here, to better illustrate the behavior of the distances over time. The dashed line indicates the threshold, $D_{\text{vis}} = .44$, below which flow fields appear visually similar, see Figure 3.1.

where $\langle \cdot \rangle_{\mathcal{R}}$ denotes the average over all $\mathbf{u} \in \mathcal{R}$. In this manner, Σ gives a characteristic "radius" of $\mathcal{R}$. We choose $\mathcal{R}$ to be lobe 1 in TCF(a) and choose $\mathcal{R}$ to be the entire chaotic set in TCF(b). We note that, in TCF(a), we also computed Σ for lobes 2 or 3 and found them to be qualitatively identical to that of lobe 1; all lobes are about the same size in the state space.

Figure 2.9 and Figure 2.10 show the normalized distance to all solutions in our libraries of TCF(a) and TCF(b), respectively. On numerically accessible timescales, turbulence never comes closer than $\sim .25\Sigma$ to any known solution, in either geometry, and turbulence clearly does not enter the linear neighborhood of these solutions. Note, however, that the threshold for visual similarity between flow fields occurs at about $D_{\text{vis}} = .4$ in TCF(a) ($D_{\text{vis}} = .44$ in TCF(b)); flow snapshots resemble each other quite well at distances below D_{vis}, as illustrated by Figure 2.11 for TCF(a). Hence, there are instances of visual similarity between turbulence and the library of ECS.

In Chapter 1, smoothness of the flow was used to prove that an infinitesimally close pass implied dynamical similarity. Here, we find that visual similarity does not imply that infinitesimal closeness. At these finite distances, there are many different situations for two trajectories to be instantaneously similar but not shadow each other, as illustrated in Fig-

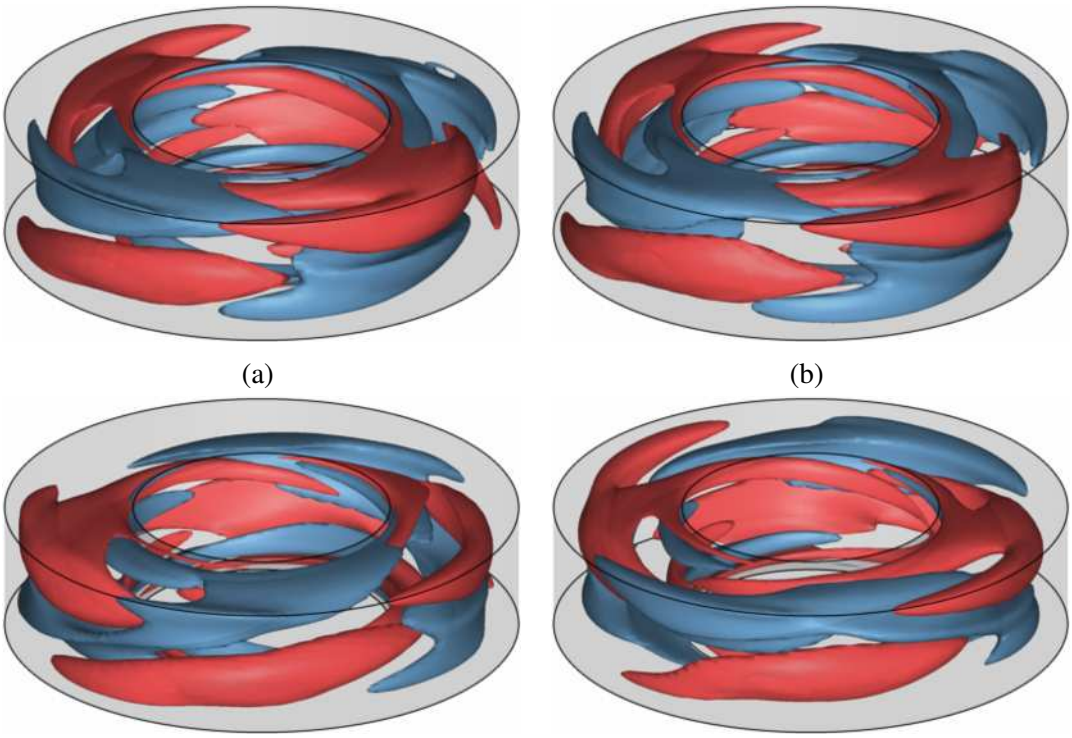

Figure 2.11: Comparison of (a) the turbulent flow field and (b) RPO_{04} at an instant where $d^{\perp} = 0.34$ is less than D_{vis}. Comparison of (c) the turbulent flow field and (d) RPO_{12} at an instant where $d^{\perp} = 0.78$ is larger than D_{vis}. To represent the flow structure in the entire flow domain, here and below, we show two level sets of u_{θ}, one with a positive value (in red) and one with a negative value (in blue). In all plots, the mean flow has been subtracted off.

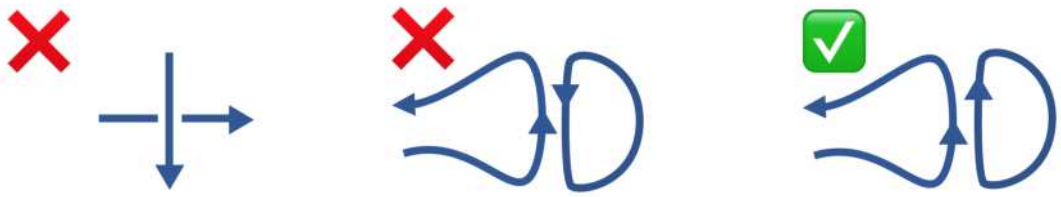

Figure 2.12: (a) Two trajectories are close for a short time interval but are not dynamically similar. (b) Two trajectories are close over an extended interval of time but are not dynamically similar. (c) Two trajectories are close over many instances and are dynamically similar.

ure 2.12. Notice that, for the configuration illustrated in Figure 2.12(a), the flow becomes non-differentiable at the intersection of the two paths in the limit the minimal distance between the paths goes to zero; the same is true for Figure 2.12(b). For smooth flows, situ-

ations like Figure 2.12(a) and (b) are disallowed between *infinitesimally* close trajectories. However, configurations like Figure 2.12(a) and (b) can occur between turbulent flow and an ECS during a "close pass," since they rarely pass infinitesimally close.

2.6 Comparison with Experiment

Recent work in our lab has investigated TCF(b) experimentally [59]. In this experimental setup, planar particle image velocimetry was used to capture two-dimensional, two-component (2D-2C) velocity data within the $z \approx 0$ cross-sectional slice of the flow domain [59]. Upon inspection, we find that, in TCF(b), distances computed from the 2D-2C velocity data approximated distances in the full state space sufficiently well. That is, the in-plane norm

$$\|\mathbf{f}\|_z = \left(\int_A \left[f_r^2(r,\theta,0) + f_\theta^2(r,\theta,0) \right] \, r dr d\theta \right)^{\frac{1}{2}} \tag{2.16}$$

is approximately proportional to the volumetric norm when applied to turbulent flow states. To illustrate this, Figure 2.13 compares $d^\perp$ computed from the volumetric norm, Equation 2.9, with $d^\perp$ computed from the in plane norm, Equation 2.16. Both time-series have been normalized to allow for a proper comparison. In this figure, a clear correlation exists between distances computed over the entire volume and distances computed with only in-plane velocities obtained from the mid-plane. Using the in-plane norm, the radius of the chaotic set is $\Sigma = 34$ ($\Sigma \approx 157$ using the volumetric norm).

The remainder of our analysis of TCF(b) will be performed using distances computed in the cross-section of constant z-height (that is, using $\| \cdot \|_z$). This is done is order to compare numerical results with those captured in experiment. However, we stress that the ability to compute distances from two-dimensional data should not be taken to imply that the flow is quasi-two-dimensional. Indeed, the small aspect-ratio Γ implies that end-cap-induced Ekman pumping strongly affects the flow over its entire axial extent, as illustrated in Figure 2.2 and Figure 2.6.

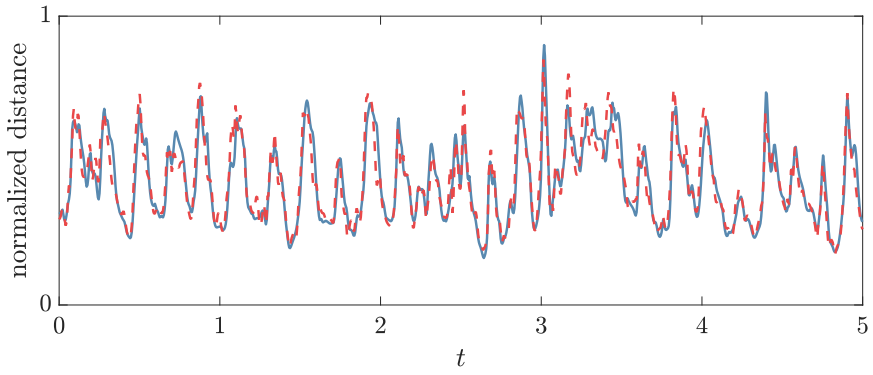

Figure 2.13: The distance $d^{\perp}$ between a turbulent flow and RPO_7 in TCF(b), computed using the volumetric norm (solid blue, Equation 2.9) as well in the in-plane norm (dashed red, Equation 2.16). Both signals were normalized to allow direct comparison. These normalized signals differ by less than 1% relative error over the non-dimensional interval $t \in (0, 60)$, indicating that the 2D-2C distance is a good proxy for distances in the full flow domain.

CHAPTER 3
SHADOWING IN TURBULENCE

Since "close passes" are not a sufficient condition for dynamical similarity between a turbulent trajectory and an ECS, shadowing must be quantified from additional metrics. To determine whether an ECS is truly dynamically relevant in this context, we need to ensure

i. that turbulent flow repeatedly visits the neighborhood of an ECS,

ii. that, when it comes "close" to an ECS, turbulent flow remains "close" over a characteristic time scale of the dynamics,

iii. that the spatial *and* temporal features of turbulent flow are well described by the ECS during this interval.

For item (ii), we use γ_n^{-1} to define a characteristic time scale for each ECSs, listed in Table 2.1 and Table 2.2. While conditions (i) and (ii) are easy to verify by direct inspection, verifying the shadowing condition (iii) requires more care.

Due to the high-dimensionality of the state space, it is often practically necessary to choose a projection in which to define shadowing, however, it must be done with care. Generic low-dimensional projections, like the $\mathcal{EHD}$-projection used in the previous chapter, can be misleading in the sense that trajectories that appear similar in projection can be arbitrarily dissimilar in the full state space.

Figure 3.1(a) plots, in a low-dimensional projection onto $\mathcal{E}$ and $\mathcal{D}$, an interval of time enclosing a shadowing event in TCF(b). The sub-interval where condition (iii) is met is illustrated in red. This projection suggests that a portion of turbulent trajectory has a shape qualitatively similar to that describing RPO_1 (shown in blue), although the ability to discriminate between when this similarity begins and ends is quite poor. One could reasonably

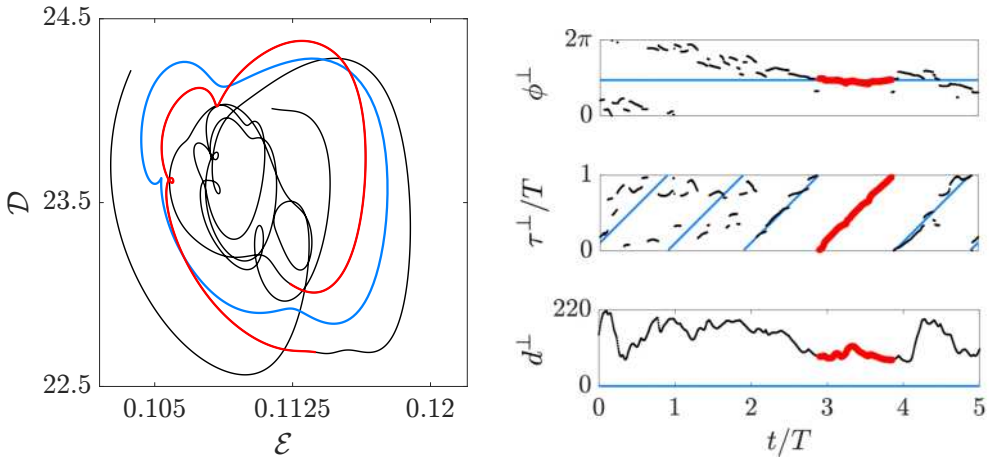

Figure 3.1: An example of shadowing, from numerical simulation of TCF(b), using different projections of state space. (a) A traditional projection onto the two-dimensional subspace spanned by the energy density $\mathcal{E}$ and dissipation rate $\mathcal{D}$ of the non-dimensional velocity fields. (b) The same interval of time, projected onto the local coordinates: azimuthal phase $\phi^\perp$, temporal phase $\tau^\perp$, and non-dimensional distance $d^\perp$. In both panels, RPO_1 is shown in blue and turbulent flow is shown in black (red) outside (inside) the shadowing interval. The interval shown corresponds to the shadowing event at $t \approx 17$ min in Figure 3.10(b).

suggest the qualitative similarity in projection continues into the right-most portion of the turbulent trajectory around $\mathcal{E} \approx .12$.

Moreover, closeness in this projection is a biased metric towards intervals where the turbulent trajectory and the ECS have similar time-series of $\mathcal{E}$ and $\mathcal{D}$, but may be far apart from each other in the full state space. This projection says nothing about the spatial similarity of the flow.

A physics-informed projection, which leverages the symmetries and geometry of the problem, is much more appropriate. Consider that, topologically, a quasi-periodic flow corresponds to a torus in state space which, in the case of an RPO, can be fully parameterized by the velocity field $R_\phi \mathbf{u}_n(\tau)$ with cyclic coordinates $\tau \in [0, T_n)$ and $\phi \in [0, 2\pi/N)$. As a result, the set of all states belonging to an RPO span the surface of a 2-torus, and all points on this torus may be parameterized by the temporal phase τ and angular phase ϕ. If we consider flow initialized at a point on the surface of this torus, $R_{\phi_0}\mathbf{u}_n(\tau_0)$, and allow τ

and ϕ to exist over the entire real line, $\mathbb{R}$, then temporal evolution is fundamentally simple in this parameterization:

$$\begin{aligned}\tau(t) &= \tau_0 + t \\ \phi(t) &= \phi_0.\end{aligned} \tag{3.1}$$

For TWs, we assert that $\phi = 0$, since motion along τ and ϕ are identical for these solutions.

Of course, on the torus, there is an equivalence of all points $(\tau - kT_n, \phi + k\Phi_n)$ with integer k; integrating an RPO forward or backwards in time by T_n time units it equivalent to rotating it by Φ_n radians. Hence, on the cyclic domains of τ and ϕ, there are discontinuities in the signals of $\tau(t)$ and $\phi(t)$ every T_n time units, as τ cycles from $\tau = T_p$ to $\tau = 0$ and ϕ accrues an added factor of Φ_n. It is possible to remove these discontinuities, as described in [16].

Trajectories $\mathbf{u}(t)$ just off the surface of this torus may be projected onto phases

$$\{\tau^{\perp}(t), \phi^{\perp}(t)\} = \arg\min_{\tau,\phi} d_n(t, \tau, \phi), \tag{3.2}$$

that minimize the distance between $\mathbf{u}(t)$ and the torus

$$d_n(t, \tau, \phi) = \|\mathbf{u}(t) - R_{\phi}\mathbf{u}_n(\tau)\|. \tag{3.3}$$

Notice that d_n evaluated at these phases, $d_n(t, \tau^{\perp}(t), \phi^{\perp}(t)) = d_n^{\perp}(t)$, is simply the minimal distance from Equation 2.14. This decomposition is a generalization of the approach proposed by Suri et al. to study the unstable manifolds of equilibria [34] and unstable periodic orbits [45]; it relies on the skew product decomposition of the dynamics [68, 69] in the vicinity of relative solutions induced by continuous symmetries. Coordinates $\tau^{\perp}$ and $\phi^{\perp}$ describe the evolution of a nearby trajectory along the group manifold of the RPO, while $d^{\perp}$ describes the evolution transverse to the group manifold.

For a trajectory lying directly on the torus, $d^{\perp} = 0$ and evolution will be described by Equation 3.1 exactly. For $d^{\perp}$-small, one would expect Equation 3.1 to be satisfied approximately. Indeed, this is what we find for the segment of the turbulent flow shown in red in Figure 3.1(b). As panel (b) illustrates, over an interval comparable to one period of RPO_1, the temporal phase $\tau^{\perp}(t)$ faithfully follows a diagonal, straight line, indicating that turbulent flow evolves at the same rate as the RPO. The azimuthal phase $\phi^{\perp}(t)$ remains nearly constant over the same interval. This linear behavior degrades harshly outside the shadowing interval, clearly demarcating where the shadowing conditions are best satisfied.

Furthermore, unlike the projection onto $\mathcal{E}$ and $\mathcal{D}$, this method retains information about the spatial and temporal similarity of the two solutions. Moments where $d^{\perp}$ are small guarantee similarity between the spatial features of turbulent flow and the ECS. In turn, instances where the phases resemble Equation 3.1 indicate that the turbulent flow and the RPO evolve similarly within the group manifold. As the dimension of a solution's group manifold increases, the approach is able to enforce temporal similarity more strictly and in a higher dimensional space. Note that ECSs can have different dimensionalities, and indeed, this approach quantifies temporal similarity more strictly when applied to RPOs than TWs (although it is a robust projection for both [16]). Hence, the evolution of $d^{\perp}$ and coordinates parametrizing the group manifold of the ECS (e.g. $\phi^{\perp}$ and $\tau^{\perp}$) are useful in defining a set of natural criteria for shadowing of an ECS.

We will consider a turbulent trajectory to shadow an RPO if, for a temporal interval $I(t) = [t - \gamma_n^{-1}/2, t + \gamma_n^{-1}/2]$, all three coordinates behave approximately as described above. Compare this to the topological shadowing detection method for proposed by Yalnız *et al.* [48], based upon persistent homology. In the topological approach, a linear low-dimensional projection is constructed, via principal component analysis, in the neighborhood of each ECS; the shapes of the curves traced out by the turbulent trajectory and the ECS in this projection are then compared via persistent homology. This approach benefits from being invariant to all continuous symmetries of the flow. Both the topolog-

ical approach, as well as the approach proposed here, first project the turbulent flow and the ECS into a local coordinate system and then compare the similarity of their trajectories in projection. The method proposed here benefits from the fact that the shape of the ECS trajectory in projection in well understood, from Equation 3.1, and as a result, does not require persistent homology to quantify similarity between the turbulent trajectory and that of the ECS; in the method proposed here, shadowing can be quantified simply from $d^{\perp}$, $\tau^{\perp}$ and $\phi^{\perp}$. Because the distance computed from persistent homology is invariant to continuous symmetries, these two methods are complimentary of each other: the topological approach is invariant to all continuous symmetries while the skew-product decomposition used here leverages them directly as a projection for the flow. One disagreement between the skew-product method and the topological method, as used in [47], is that the topological method enforces shadowing for a full period, which contradicts Property **S2**. In constrast, the method proposed here only requires shadowing for intervals of length γ_n^{-1}. However, the topological approach could easily be augmented to detect shadowing over other interval lengths with virtually no changes.

We will propose two numerical algorithms for detecting when an interval $I(t)$ meets criteria (i-iii). In method 1, we evaluate an error from $\tau^{\perp}$ and $\phi^{\perp}$. That is, we evaluate an error from the normalized deviation

$$\begin{aligned} E_{\tau}(t) &= \min_{\tau_0} \frac{1}{T\gamma_n^{-1}} \int_{I(t)} |t' + \tau_0 - \tau^*(t')|^2 dt' \\ E_{\phi}(t) &= \min_{\phi_0} \frac{1}{(\pi/N)\gamma_n^{-1}} \int_{I(t)} |\phi_0 - \phi^*(t')|^2 dt' \end{aligned} \tag{3.4}$$

of phases $\tau^{\perp}(t)$ and $\phi^{\perp}(t)$ away from their expected behavior Equation 3.1. Here,

$$\begin{aligned} \tau^{\perp}(t) &= \tau^*(t) \mod T_n, \\ \phi^*(t) &= \phi^{\perp}(t) \mod \Phi_n, \end{aligned} \tag{3.5}$$

is an appropriately chosen transformation to remove the discontinuities in $\tau^{\perp}(t)$ and $\phi^{\perp}(t)$ [16].

Both errors being simultaneously small indicate an interval within which conditions (ii) and (iii) are satisfied. To satisfy condition (i), we also require that the error [1]

$$E_{\text{vis}}(t) = \max_{t' \in I(t)} \frac{d^{\perp}(t')}{\Sigma} \tag{3.6}$$

be less than D_{vis}. In other words, we require the turbulent flow and the ECS to be visually similar for the entire interval.

Method 2, in contrast, computes an error solely from distance. That is, we scan $d_n(t, \tau, \phi)$ for instances where τ and ϕ evolve exactly as described in Equation 3.1 and compute an error from the mean normalized distance over the interval,

$$E_d(t) = \min_{\tau_0, \phi_0} \frac{1}{\gamma_n^{-1}} \int_{I(t)} \frac{d_n(t', \tau(t'), \phi(t'))}{\Sigma_n(\tau(t'), \phi(t'))} dt', \tag{3.7}$$

where Σ_n is a local length scale for distance in the neighborhood of ECS n. Instances where E_d is small indicate intervals of time where all three conditions (i-iii) are satisfied.

A characteristic distance scale can vary substantially throughout state space, as the density of trajectories in state space itself varies; this characteristic distance can even vary along a single recurrent solution. Consider TCF(b), whose attractor has a characteristic spike in energy approximately every $.235$ non-dimensional time-units. During these spikes, the proper velocity scale—and thus distance scale—will be slightly higher than average. Hence, a normalized distance, E_d, should use a larger distance scale for portions of ECSs lying in this high energy region.

In general, a local length scale may be computed as the harmonic mean distance be-

[1] It would be more appropriate and consistent with method 2 to normalize by $\Sigma_n(\tau^{\perp}(t'), \phi^{\perp}(t'))$ in Equation 3.6. However, we published method 1 in TCF(a) before ever finding the need for such a scaling in TCF(b). To be consistent with [16], we use Σ here.

tween turbulent flow and a given RPO,

$$\Sigma_n(\tau,\phi) = \left[\frac{1}{T}\int_0^T \frac{dt}{\|\mathbf{u}(t) - R_\phi \mathbf{u}_n(\tau)\|}\right]^{-1}, \tag{3.8}$$

where T is the duration of the turbulent trajectory. A harmonic mean weighs small distances more than would an arithmetic mean and thus provides a more local measure of the characteristic distance to the RPO. In general, Σ_n will not depend on coordinates related to symmetries of the governing equations, but may rely on the those that aren't. The continuous rotational symmetry of the governing equations implies that Σ_n must be rotationally symmetric and have no ϕ dependence. In constrast, the symmetry of the ECSs in time is not a globally held symmetry, and it is expected that Σ_n varies in τ.

In practice, method 1 is faster and less memory intensive, since only $\tau^\perp(t)$, $\phi^\perp(t)$, and $d^\perp(t)$ need be stored, rather than the three-dimensional distance function, $d_n(t,\tau,\phi)$. However, experimental noise can cause jitter in the calculation of $\tau^\perp$ and $\phi^\perp$, leading to false negatives in the detection of shadowing when using method 1 in experiment. When it comes to experimental data, method 2 is much more robust. For this reason, we explore method 1 in TCF(a), and method 2 in TCF(b) where we compare with experiment. Note that method 1 is used in [16] and [56], and method 2 is introduced in [57].

3.1 Results of Method 1 in TCF(a)

In TCF(a), we find convincing evidence of shadowing using thresholds

$$E_\tau < 10^{-4} \qquad E_\phi < 3\times 10^{-4} \qquad E_{\text{vis}} < .4 \tag{3.9}$$

For TWs, shadowing is determined by entirely by E_τ and E_{vis}.

Figure 3.2(a) and (b) illustrate a summary of all shadowing intervals found for (a) a turbulent trajectory that explores lobes 1 and 2 (blue in Figure 2.3) and (b) and a turbulent trajectory that explores lobe 3 (red in Figure 2.3). In the former case, we find that turbulent

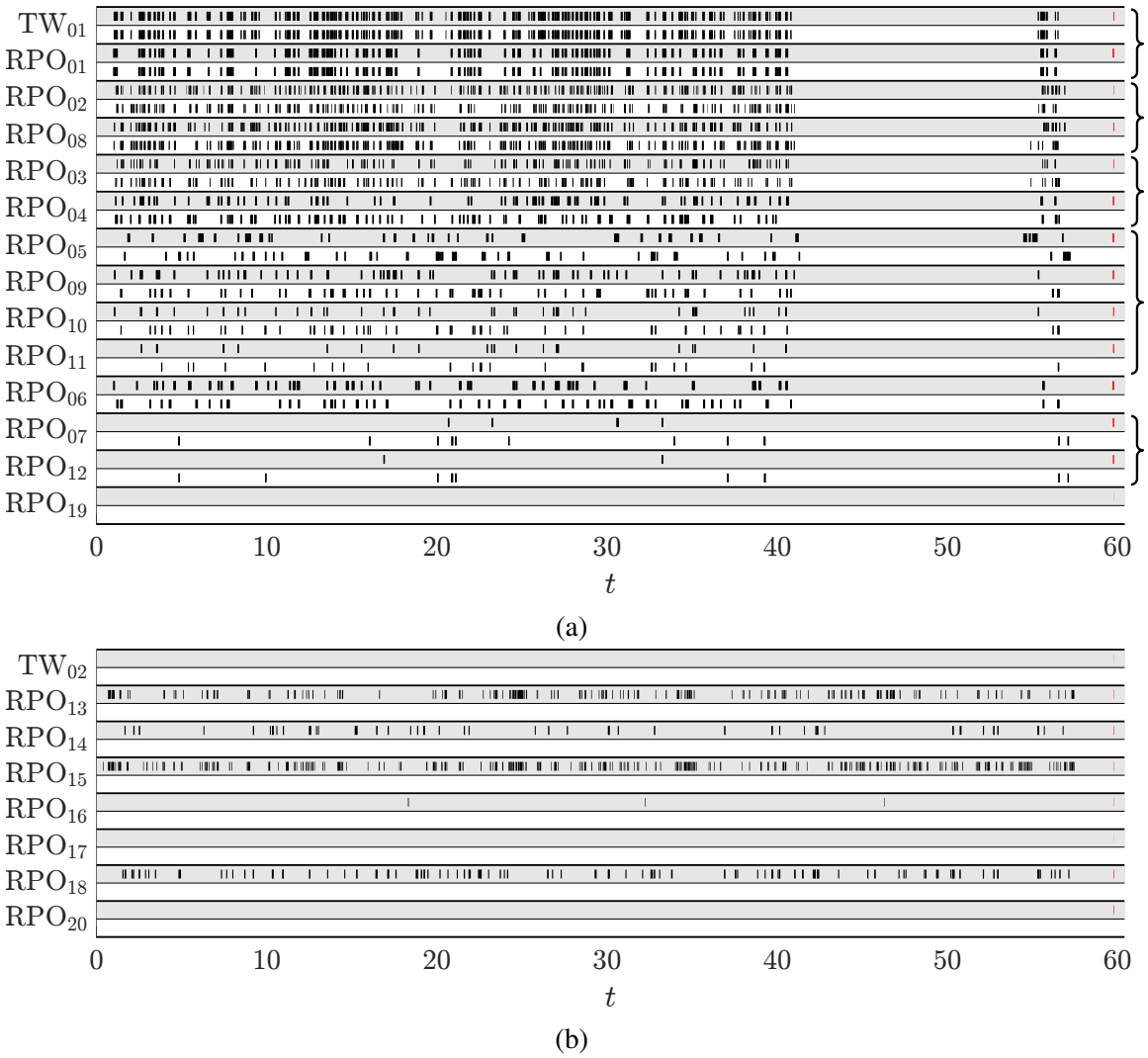

Figure 3.2: A summary of the shadowing events (marked with black bars) for turbulent trajectories that explore (a) lobes 1 and 2 and (b) lobe 3. Each ECS is represented by two rows, one for the numerically converged solution $\mathbf{u}_n$ (gray) and one for its symmetric copy $K_z\mathbf{u}_n$ (white). Red bars on the right represent the escape times γ_n^{-1} to scale. Curly braces on the far right group together RPOs that are related via continuation in Re_i.

flow shadows both RPOs and a TW. Moreover, Figure 3.2 shows that if an ECS is shadowed, then so is its reflected copy. This suggests that turbulent flow in TCF(b) does not break reflection symmetry in a statistical sense, i.e., the probability of shadowing any ECS is comparable to the probability of shadowing its reflected copy. This is expected, seeing as lobe 1 is at least approximately K_z-symmetric.

Consider an observed shadowing event to RPO_{05} shown in Figure 3.3 and its symmetry-related copy in Figure 3.4 (the corresponding movies may be found in publication [16]). The same format is used here and below to illustrate shadowing events. Figure 3.3(a) shows the evolution of $\tau^{\perp}$, $\phi^{\perp}$, and $d^{\perp}$ with black (white) circles indicating instances when the corresponding errors E_τ and E_ϕ are small (not small) and when the instantaneous distance $d^{\perp}/\Sigma$ is less (greater) than E_{vis}. Red lines denote the temporal intervals in which the criterion from Equation 3.9 are satisfied; for an interval to be considered an instance of shadowing, all three criteria must be met simultaneously. The gray bar shows the length of the interval γ_n^{-1} for comparison with the temporal period of the ECS. Panels (b) and (c) compare, respectively, the spatial structure (contours of constant u_θ at the values denoted in yellow on the color bar in panels (d) and (e)) of the turbulent flow and the corresponding ECS in the entire domain at the instant denoted by the vertical black line in panel (a). Finally, panels (d) and (e) compare the velocity fields in the yellow cross-section shown in panels (b) and (c), respectively. In all panels, the turbulent mean flow is subtracted off.

Note that, for both RPO_{05} and its symmetry-related copy, the respective RPO is shadowed continuously for several periods (interval of around $6\gamma_n^{-1}$). During the shadowing intervals, all three criteria are satisfied to a high accuracy: the evolution of $\tau^{\perp}(t)$ and $\phi^{\perp}(t)$ is given approximately by Equation 3.1 and the normalized distance stays almost always below the threshold. As discussed previously, turbulent flow is visually almost indistinguishable from the corresponding ECS in the entire domain when the normalized distance is below threshold. Figure 3.3(b-c) illustrates this particularly convincingly for RPO_{05}.

It is expected that, for small $d^{\perp}(t)$, the turbulent flow evolves in the same manner as the

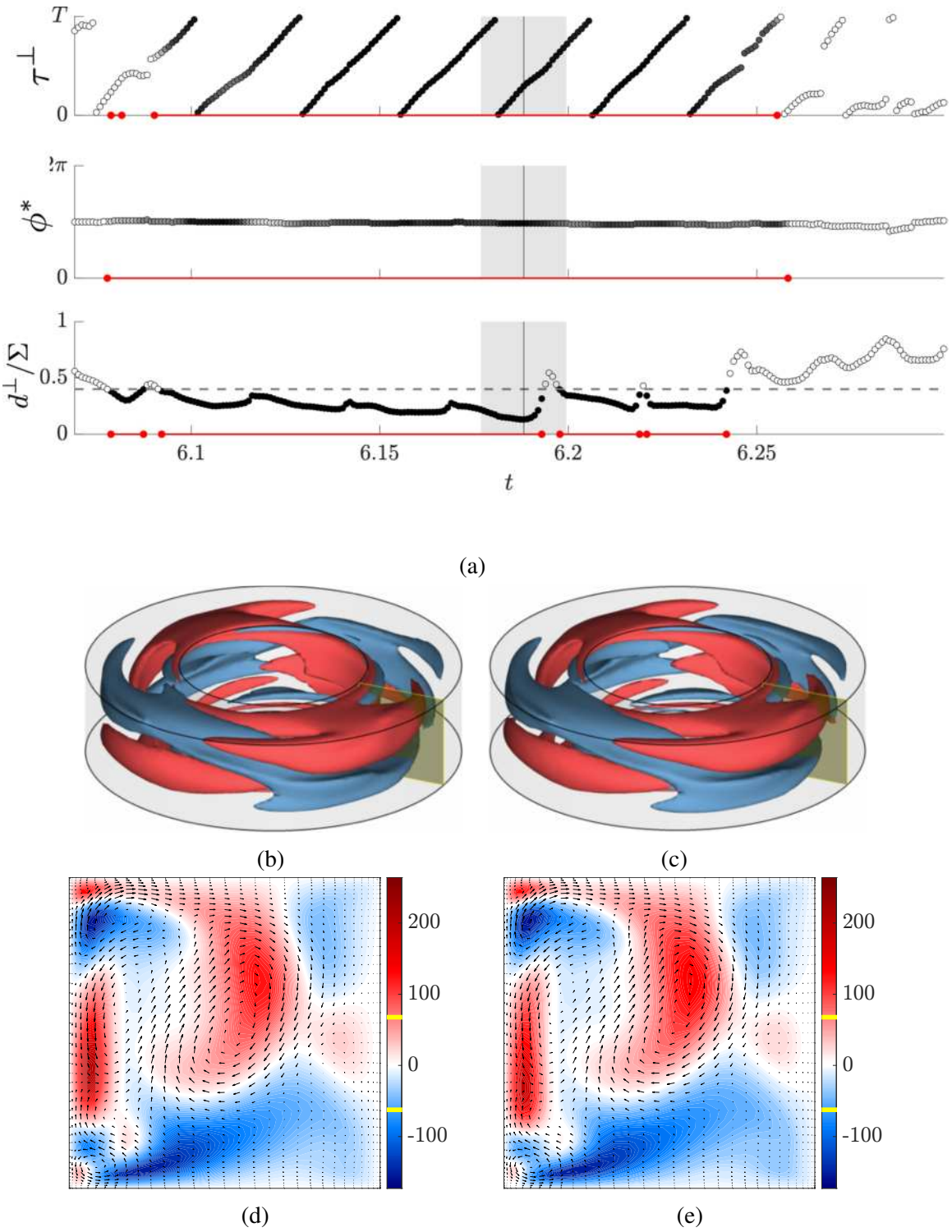

Figure 3.3: Turbulent flow shadowing RPO_{05} in lobe 1. (a) Evolution of coordinates τ, $\tilde{\phi}$, and D. Black (white) circles indicate instances when the corresponding shadowing criterion is satisfied (not satisfied). Red lines denote the temporal intervals during which a given criterion is satisfied. The gray bar shows the escape time, γ_n^{-1}. Snapshots of (b) the turbulent flow and (c) the ECS at the instant marked with the black vertical line in (a). Flow fields in the yellow cross-section for (d) the turbulent flow and (e) the ECS. A movie of this shadowing event is published [16].

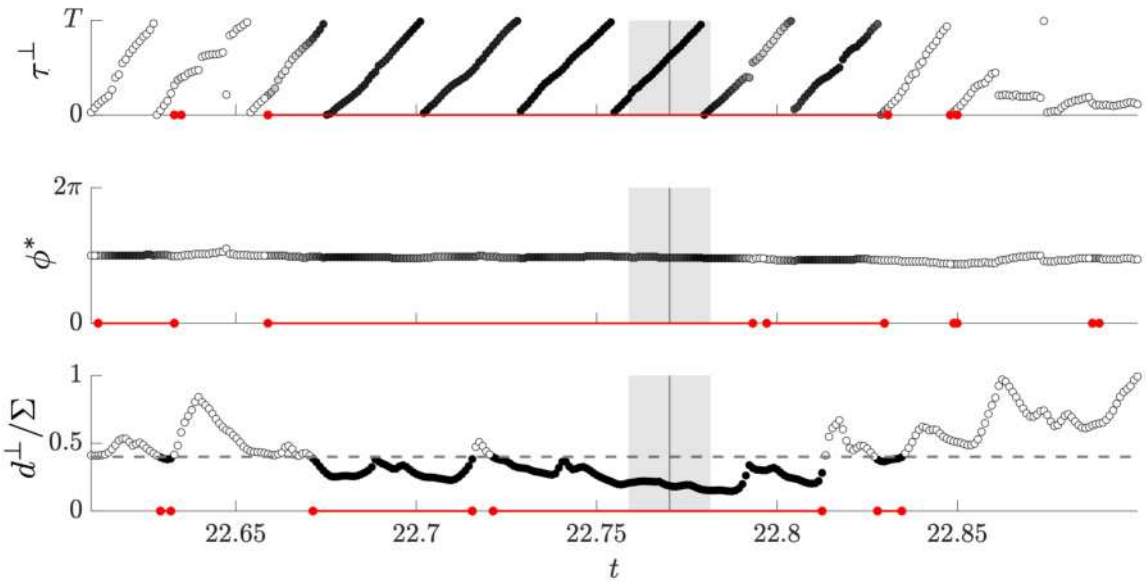

(a)

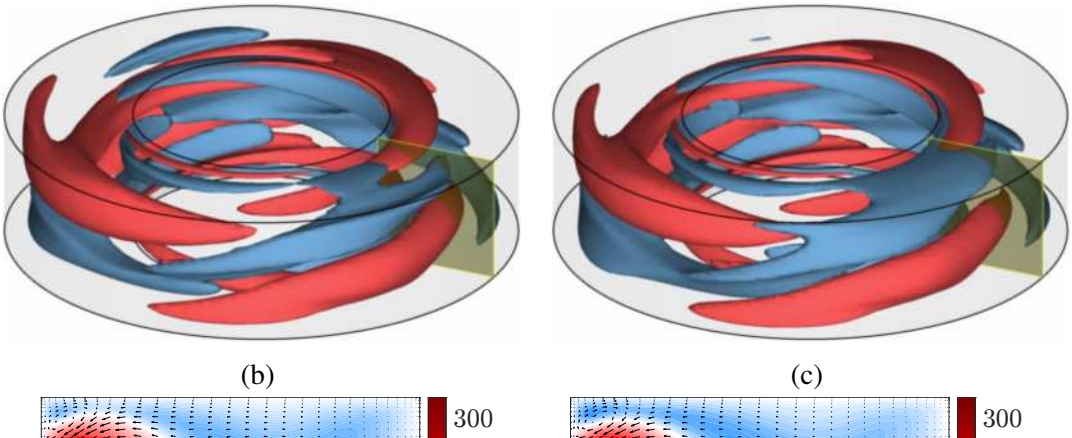

(b) (c)

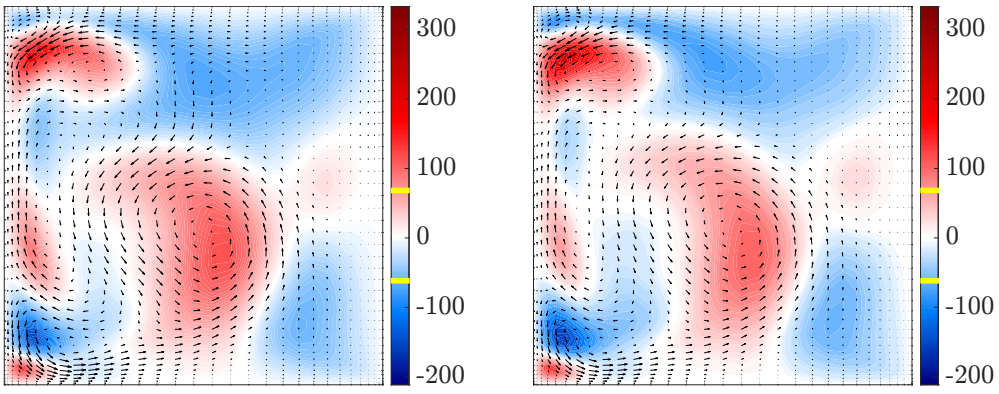

(d) (e)

Figure 3.4: A shadowing event for the reflected copy of RPO_{05} in lobe 1. A corresponding movie is available in the publication [16].

nearby RPO. However, temporal similarity appears to persist even through instances where spatial similarity in broken. As seen in Figure 3.3, even when $d^{\perp}(t)/\Sigma$ briefly exceeds D_{vis}, the slopes of $\tau(t)$ and $\phi(t)$ remain virtually unchanged, suggesting that turbulent flow continues shadowing the same member of the RPO family even when the corresponding flows become visually dissimilar. Analogous statements apply to the reflected version of RPO_{05}, as Figure 3.4 illustrates.

Figure 3.5 presents a sequence of several shadowing events for RPO_{01}. These shadowing events are of duration comparable to those for RPO_{05} and its reflection, measured in units of γ_n^{-1}, but correspond to quite a few periods of RPO_{01}. Not only that, turbulent flow also visits the neighborhood of RPO_{01} much more frequently, as Figure 3.2(a) demonstrates. In fact, this solution is by far the most frequently visited RPO in lobe 1. Note that RPO_{01} is symmetric with respect to $K_z R_{\pi/2}$, so reflection is equivalent to a rotation by $\pi/2$. Hence, both RPO_{01} and its reflection belong to the same solution family, and both rows in Figure 3.2(a) contain identical sequences of shadowing events. Also, just like in the case of RPO_{05}, turbulent flow is essentially indistinguishable from RPO_{01} during the shadowing episodes.

Figure 3.6 illustrates shadowing of TW_{01}. Rather unexpectedly, TW_{01} is found to be shadowed even more frequently than RPO_{01}. In fact, when the turbulent trajectory is inside lobe 1, it spends more time near TW_{01} than any other ECS according to Figure 3.2(a). Moreover, when TW_{01} is shadowed, then typically so is RPO_{01}. This is not particularly surprising, as RPO_{01} is rather compact, and the two ECSs lie very close to each other. This is a consequence of RPO_{01} being born in a Hopf bifurcation of TW_{01} [16], which happens to lie close in the parameter space. It should also be mentioned that the length of the shadowing intervals for TW_{01} tends to be quite large (e.g., around $8\gamma_n^{-1}$ for the event shown in Figure 3.6) compared with typical shadowing intervals for the RPOs embedded in lobe 1.

We have not found any shadowing events for RPO_{19} or its reflection, since the smallest

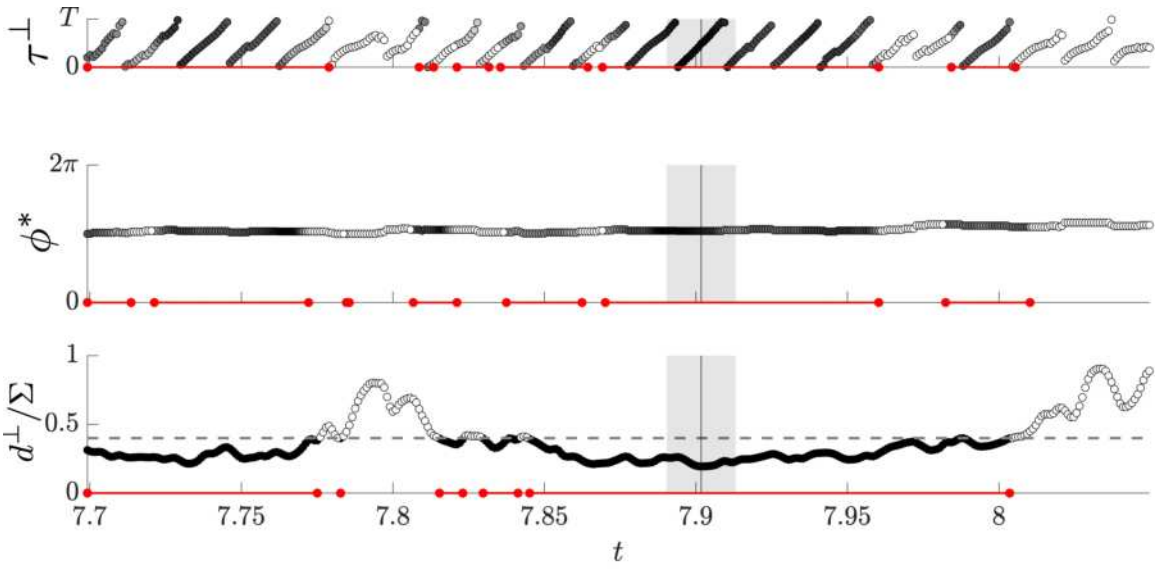

(a)

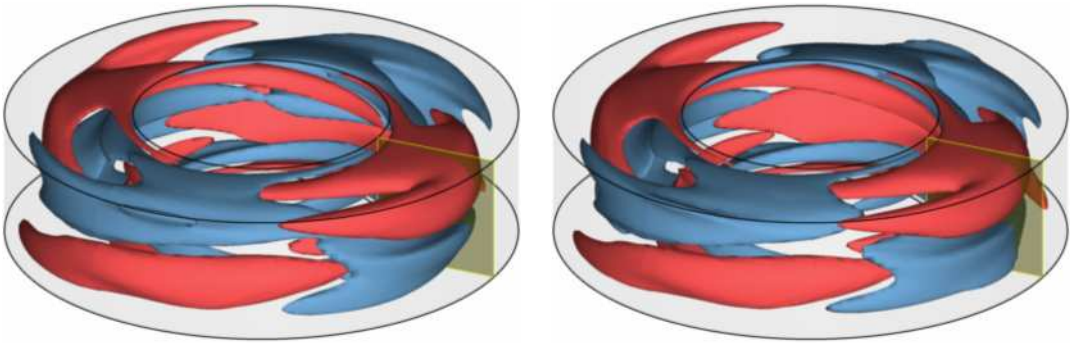

(b)

(c)

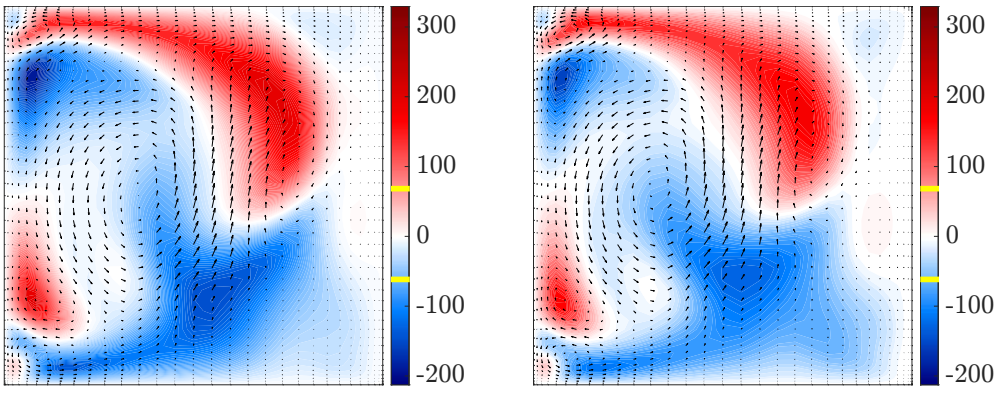

(d)

(e)

Figure 3.5: A shadowing event for RPO_{01} in lobe 1. A corresponding movie is available in the publication [16].

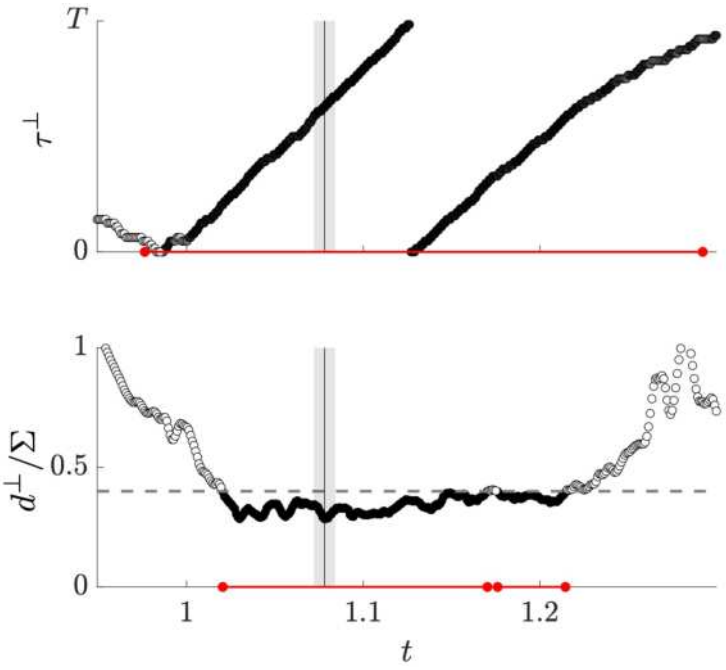

(a)

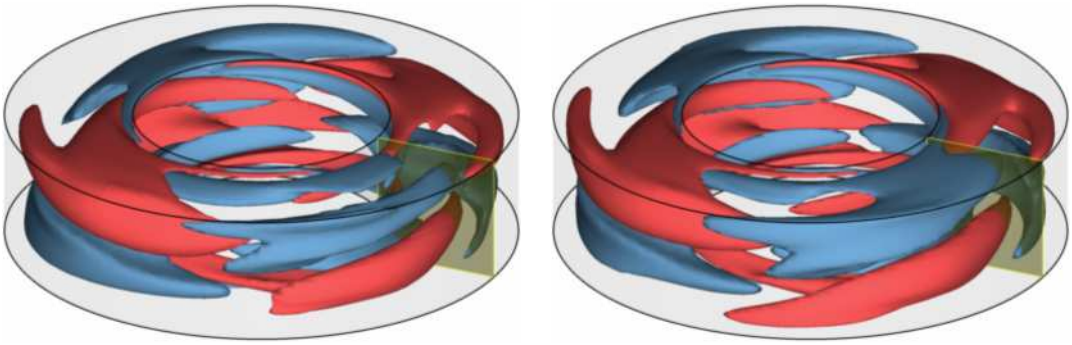

(b) (c)

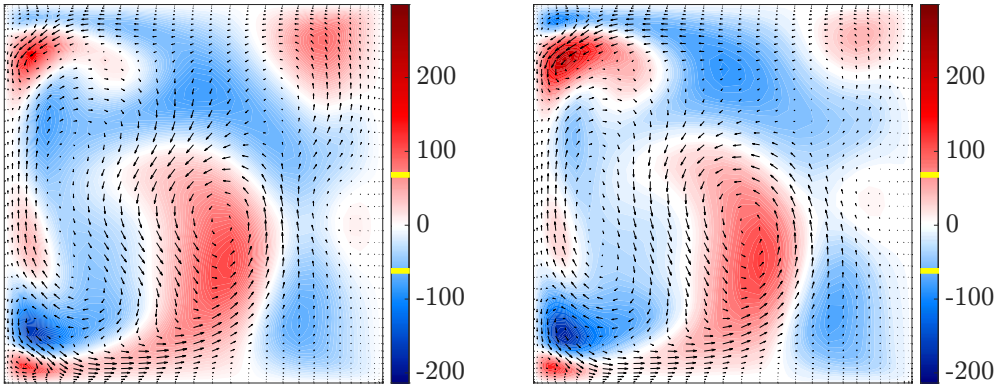

(d) (e)

Figure 3.6: A shadowing event for TW_{01} in lobe 1. A corresponding movie is available in the publication [16].

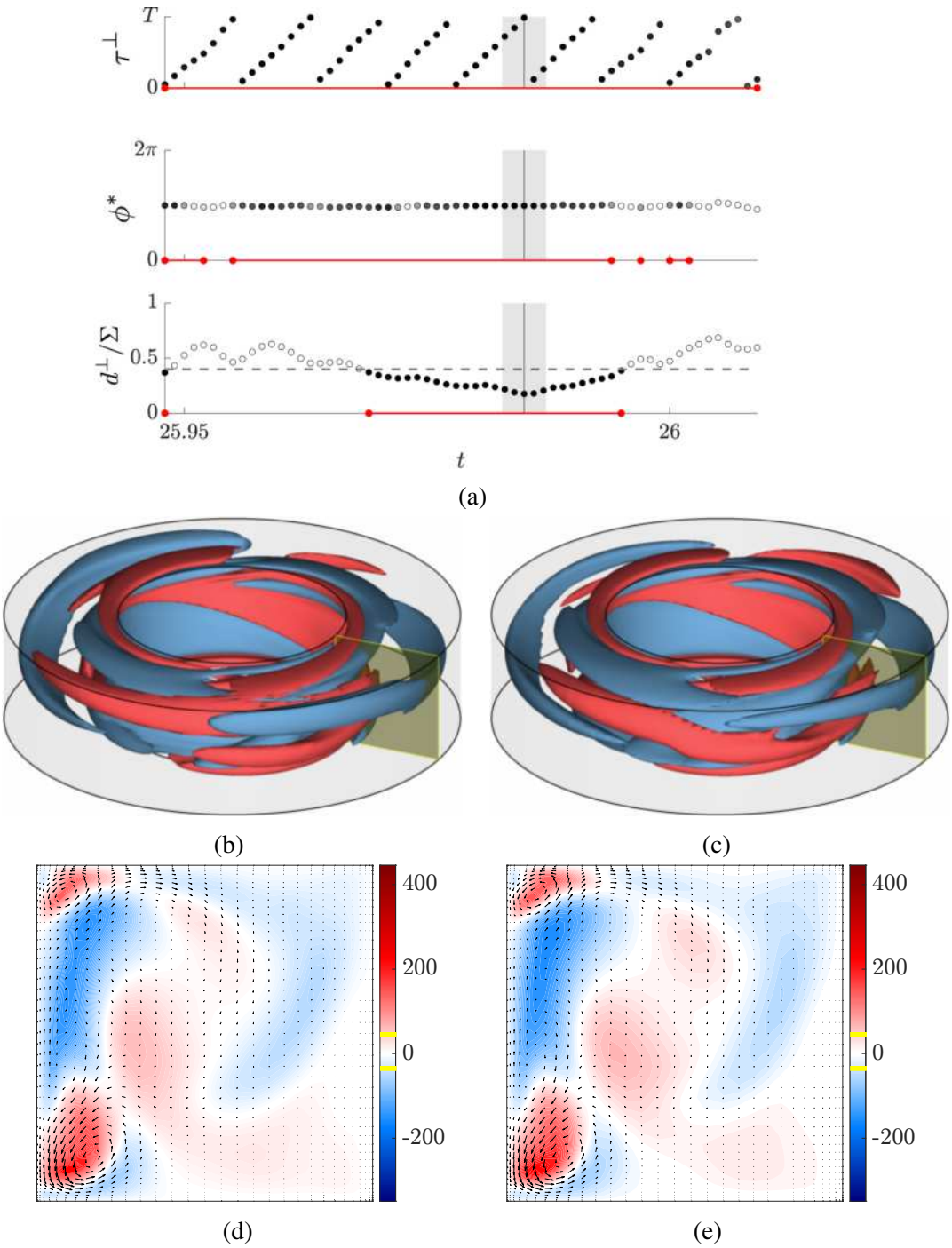

Figure 3.7: A shadowing event for RPO_{15} in lobe 3. A corresponding movie is is available in the publication [16].

observed distances $d^{\perp}/\Sigma$ for this ECS is 0.42, which fails to satisfy our shadowing criteria. Every other ECS embedded in lobe 1 is found to be shadowed by the turbulent flow. Recall

that the trajectory used to compute Figure 3.2(a) visits both lobes 1 and 2; as expected, shadowing events are confined to the temporal intervals when turbulent flow is inside lobe 1. The shadowing criteria (a)-(c) are not satisfied when the turbulent trajectory is inside lobe 2 as we have not identified ECSs in that region of the state space.

For completeness, we have also performed a similar analysis for a turbulent trajectory that explores lobe 3. It was found to shadow RPO_{13}-RPO_{16}, and RPO_{18}. Since this lobe breaks the reflection symmetry, none of the reflected copies of these RPOs were shadowed. An example of shadowing for RPO_{15} is shown in Figure 3.7. It is worth emphasizing that ECSs in lobe 3 are more unstable than those in lobe 1, as illustrated by both the larger number of unstable directions and the shorter escape time. As a result, there are fewer instances of shadowing and each shadowing event is nominally shorter. For instance, even though RPO_{15} is shadowed for almost three (very short) periods in Figure 3.7, this interval corresponds to only 0.022 in non-dimensional units, compared with around 0.1 for RPO_{01} and RPO_{05}.

3.2 Results of Method 2 in TCF(b)

Recall that, to facilitate a comparison with experiment, all norms in this section are computed in the $z = 0$ plane, impacting d_n (see Equation 3.3) and Σ_n (see Equation 3.8). The dependence of Σ_n on τ and ϕ can be seen from plotting their marginal averages

$$\langle \Sigma_n(\tau, \cdot) \rangle = \frac{1}{2\pi} \int_0^{2\pi} \Sigma_n(\tau, \phi') d\phi' \tag{3.10}$$
$$\langle \Sigma_n(\cdot, \phi) \rangle = \frac{1}{T_n} \int_0^{T_n} \Sigma_n(\tau', \phi) d\tau'.$$

As illustrated by Figure 3.8, we observe variation in τ but practically no variation in ϕ. The variation that is present in ϕ is due to T being finite in Equation 3.8.

Figure 3.9 plots E_d over the interval enclosing the shadowing event discussed in Figure 3.1. Similar to TCF(a), we observe that 0.44 provides a threshold of visual similarity

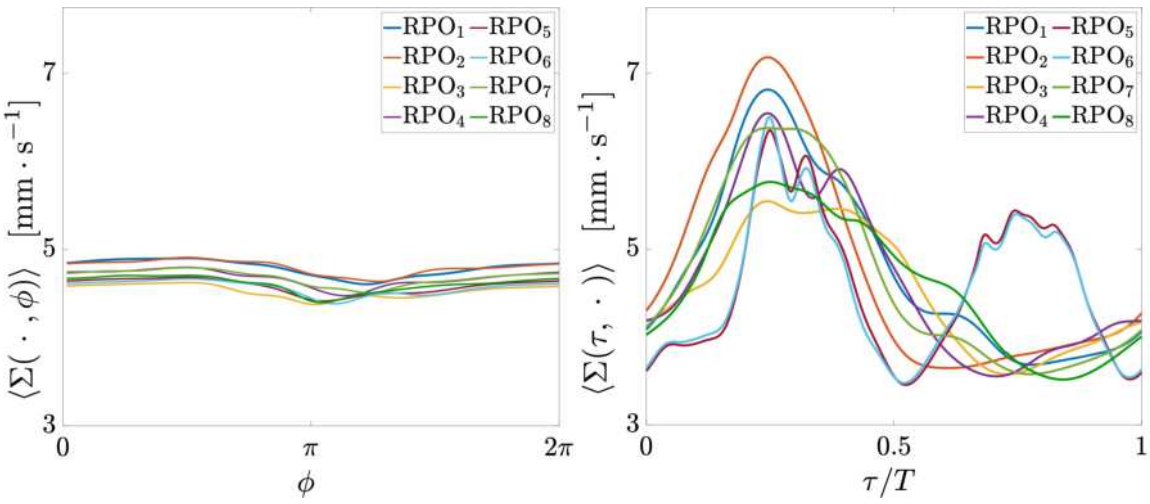

(a) (b)

Figure 3.8: The distance scale (Equation 3.8) is measured in experiment and averaged over (a) τ and (b) ϕ as described in Equation 3.10. These values may be non-dimensionalized using the velocity scale $\nu/w \approx 0.0754$ mm $\cdot$ s^{-1}.

between the flow fields in numerics. In method 2, the distance is only required to be below D_{vis} on average over the duration of shadowing. This is much less rigid constraint on the distance than that used in method 1. In method 2, shadowing intervals may include slight excursions above D_{vis}, as seen in Figure 3.3, so long as the distance is sufficiently small for the remainder of $I(t)$.

Figure 3.10 plots E_d over time for each RPO, both in (b) simulated turbulent flow and (c) two experimental observations of turbulent flow acquired by Crowley [59]; this plot may be considered the method 2 analog to Figure 3.2. Note that since the dynamics of TCF(b) spontaneously break the K_z-symmetry, there is only one row per ECS. The colorbar is chosen in each panel such that white indicates when E_d is above threshold. For simulated turbulent flow we use $E_d \lesssim .44$; experimental noise increases d_n, yielding a higher threshold value to $E_d \lesssim .47$.

For reference, method 1 was also applied to the simulated data in TCF(b) and plotted in Figure 3.10(a). The two methods presents slightly different pictures of the shadowing events, but overall they are in agreement, especially for shadowing events of high quality. Method 2 plots the quality of shadowing non-discretely. In contrast, the binary nature of

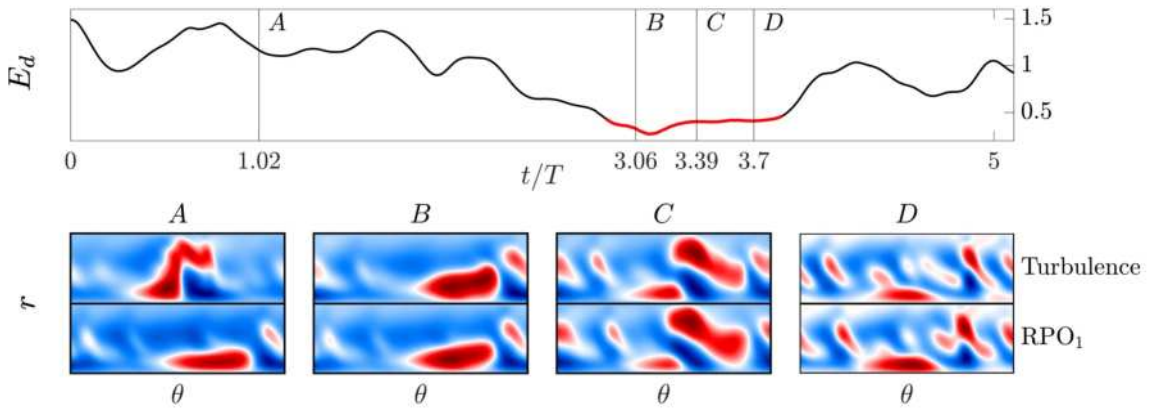

Figure 3.9: Comparison of the flow fields representing turbulent flow and relative periodic orbit (RPO$_1$) during the same interval of numerical simulation illustrated in Figure 3.1. (Top) The error E_d, with the shadowing portion shown in red. (Bottom) The flow fields corresponding to the time instances are labeled with vertical lines in the top panel. Here and below, the mean-subtracted azimuthal velocity is plotted for turbulent flow and the corresponding RPO, where red (blue) is positive (negative). Each rectangular box represents the annular region spanned by r and θ, where r_i is on the bottom and r_o is on the top.

the error E_{vis} renders method 1, in turn, binary.

The cumulative probability $P(E)$, which defines the likelihood that $E_d(t) < E$ over all RPOs and over all times, is plotted in Figure 3.11(a). The 33$^{\text{rd}}$ percentile is found to correspond to $E_0 = 0.44$ for the numerical data set and, on average, $E_0 = 0.57$ for the two experimental data sets. As demonstrated by Figure 3.9, events in this percentile show striking visual similarity between turbulent flow and the recurrent solutions. We consider the relative frequency,

$$f_n = \frac{P_n(E_0)}{\sum_i P_i(E_0)}, \tag{3.11}$$

with which each solution is shadowed in the 33$^{\text{rd}}$ percentile. Here, $P_n(E_0)$ is the probability that the error E_d is below E_0. We find the distribution of f_n to be comparable between numerical turbulence and both experimental data sets, as illustrated by Figure 3.11(b), suggesting that statistical contribution of different recurrent solutions in experiment and numerical simulation is the same.

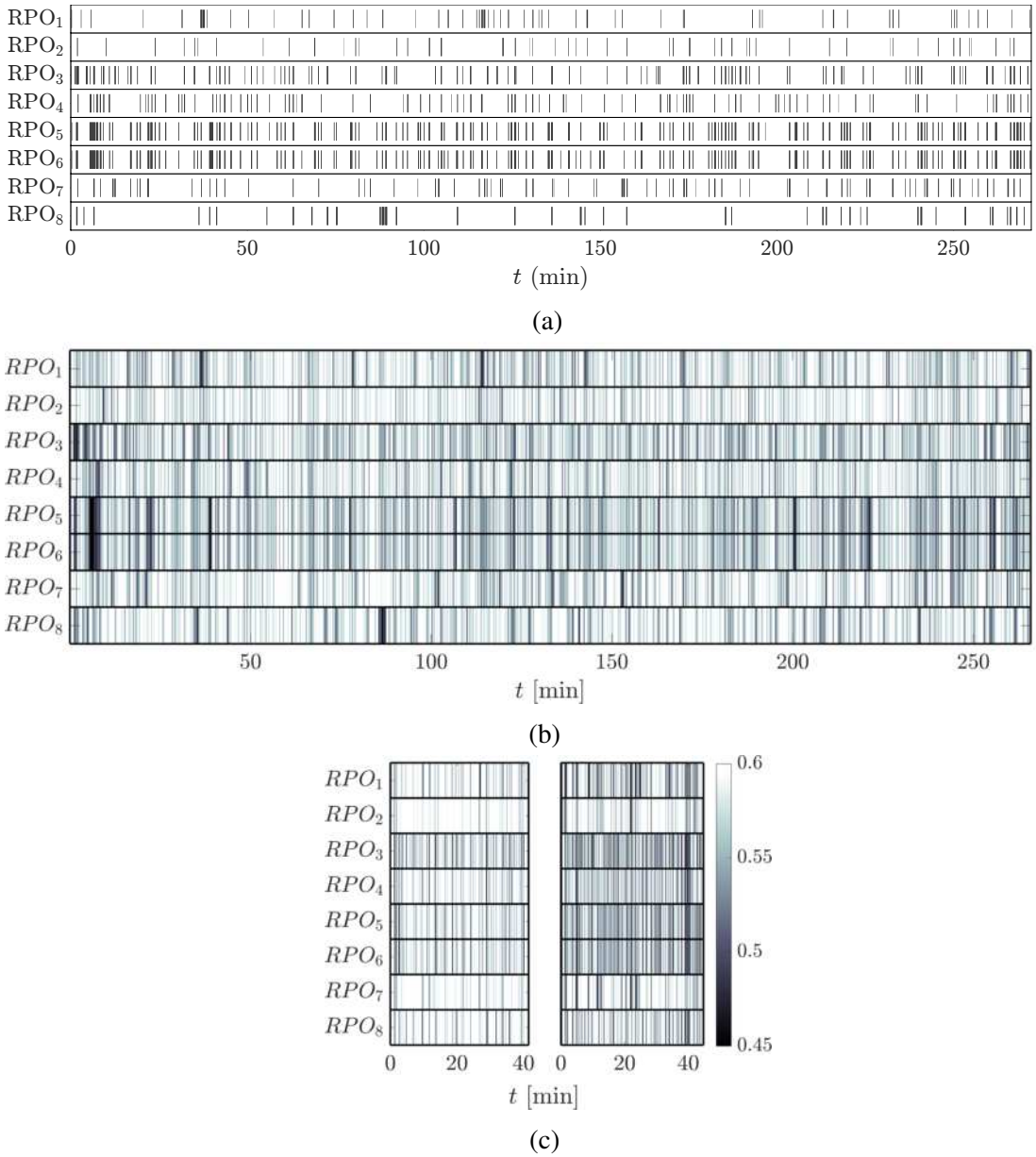

Figure 3.10: Turbulence frequently shadows relative periodic orbits (RPOs) in (a-b) numerical simulation and (c) experiment. (a) same as Figure 3.2. (b-c) For each RPO, E_d is plotted as a function of time using a color gradient; darker vertical lines indicate better quality shadowing events. Two seperate runs are shown in experiment, of roughly equal length. A slight difference in noise floor is notable between data sets. Time may be non-dimensionalized by the viscous timescale $w^2/\nu \approx 271$.

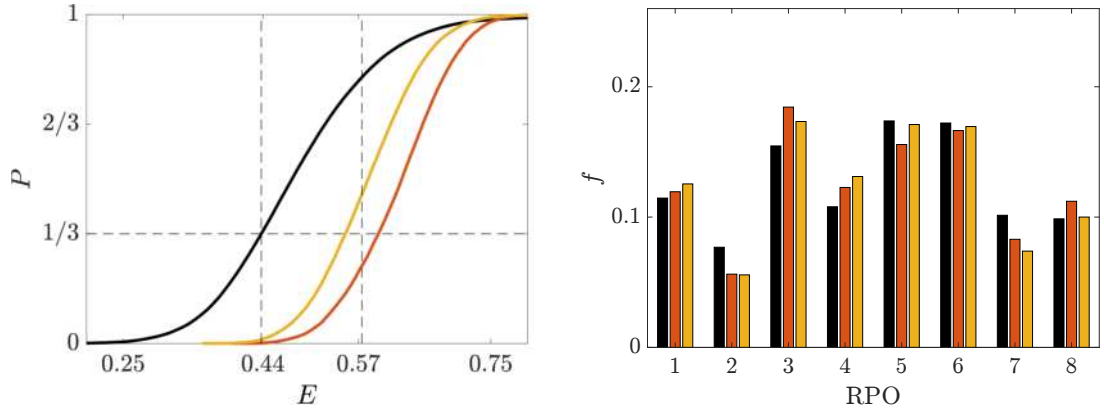

(a) (b)

Figure 3.11: (a) Cumulative probability of E_d for the numerical data set (black), and the two experimental data sets (red and yellow, respectively). A horizontal dashed line denotes the 33^{rd} percentile and vertical dashed lines represent the corresponding distance threshold for numerics and experiment. (b) The shadowing frequency f_n is plotted for each of the eight RPOs. The same color palette as in panel (a) is used to denote the three data sets.

As observed in TCF(a), turbulent flow often shadows more than one solution at once in TCF(b). Hence, turbulent flow may be described by multiple solutions simultaneously, as illustrated by Figure 3.10 and evidenced by Figure 3.12. This observation is rather surprising, given the small size of the RPO library. One might expect turbulent flow to shadow multiple solutions if these solutions are born from a nearby bifurcation in parameter space and, consequently, are themselves almost indistinguishable. This is the case for RPO_5 and RPO_6, as discussed in Chapter 2. Indeed, these two solutions are almost always shadowed simultaneously, which is unsurprising given their proximity in state space, as can be seen in Figure 3.13(a).

However, it is also possible for turbulent flow to simultaneously shadow RPOs which are not related through a nearby bifurcation, as long as portions of these RPOs lie close in state space. Figure 3.12 illustrates an example of this simultaneous shadowing in physical space; both RPO_3 and RPO_8 describe the spatial structure of turbulent flow and its evolution over an interval of 30 seconds. In this interval, the turbulent flow is similar to both RPO_3 and RPO_8 in the state space, as suggested by Figure 3.13(b). In fact, RPO_3 and RPO_8 effectively shadow each other during this interval as well.

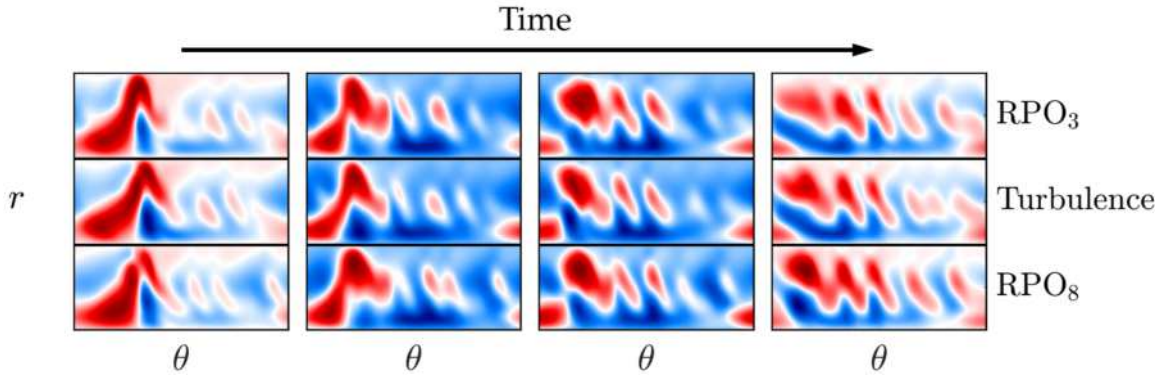

(a)

Figure 3.12: Example from numerical simulation of turbulent flow (middle) shadowing both RPOs 3 (top) and 8 (bottom) for $t \in (15\ \text{s}, 40\ \text{s})$. The timestamp of each column of panels increases from left to right. The inner three rows display shadowing between all three solutions. Notice that, when turbulent flow shadows multiple solutions, it resembles all solutions it shadows. During such intervals, the recurrent solutions may also be considered to shadow each other. Time may be non-dimensionalized by the viscous timescale $w^2/\nu \approx 271$.

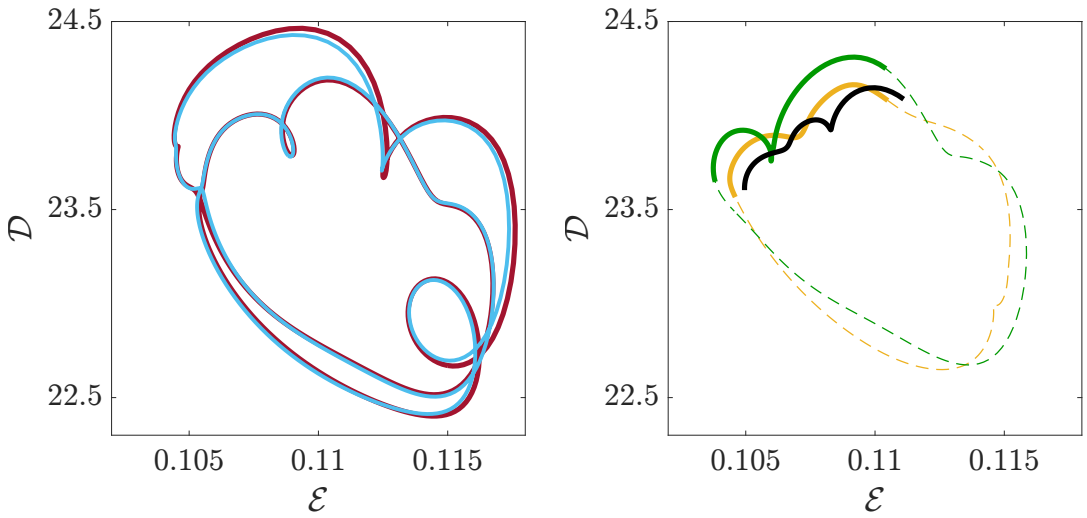

(a) (b)

Figure 3.13: Low dimensional projections of (a) RPO$_5$ (deep red) and RPO$_6$ (light blue) and (b) RPO$_3$ (yellow) and RPO$_8$ (green) in the state space. Volumetric kinetic energy and dissipation of the velocity field are used as coordinates. In (b) the intervals of each RPO that are displayed in Figure 3.12 are bolded and a segment of numerical turbulent flow shadowing these segments is overlaid in black.

CHAPTER 4
DISCUSSION AND OUTLOOK

The results presented here provide perhaps the most convincing evidence to date that turbulent flow shadows ECSs across multiple flow geometries. This work has built upon the original work of Suri *et al.* [34] and culminated in a powerful methodology for quantifying shadowing in turbulence, one that does not require ECSs to be dense nor for turbulence to come particularly close to them.

In summary, we have generalized the Axiom A notion of shadowing to turbulence and provided clear evidence that turbulence can be decomposed as a sequence of intervals well-approximated (in space and time) by unstable recurrent solutions of the Navier-Stokes equation; basically, that ECSs serve as a backbone for turbulence [70]. The shadowing property allows us to forecast turbulence in novel ways and justifies the use of an ECS-based framework to overcome the devastating effects of chaos on our ability to predict, control, and engineer fluid flows. The ability to detect shadowing is crucial for implementing reduced descriptions of turbulence, for instance, through a symbolic dynamics [71] and further development of a dynamical framework based on invariant sets [16, 56, 29, 48] could eventually enable a statistical description as well. Indeed, invariant sets such as equilibria, periodic orbits, etc., collectively define a network-like "road map" of turbulence and, with shadowing, we now have the ability to quantitatively establish where turbulence visits on this network.

If ECS describe the nodes of this network, then heteroclinic connections—dynamical transitions between ECSs—are network edges. Heteroclinic connections have been observed to be shadowed by Suri *et al.* [29] and used to generate a partial, network-like representation of the dynamics of quasi-two-dimensional turbulence. A network representation of the state space could novel insight into fluid motion, over time scales much larger

than γ^{-1}. Quite recently, a method was proposed for forecasting the propagation of small perturbations through networks [72]. In combination with such network-based methods, the shadowing detection method explored here could have profound implications on the forecasting and control of fluid flows.

However, identifying the underlying network of invariant sets is computationally taxing. Between N ECS are potentially as many as $2N^2$ heteroclinic connections, and they can be quite difficult to converge [73]. A more practical approach, perhaps, would be to explore constructing network edges from non-invariant sets. More specifically, nowhere in Chapter 3 did we require the trajectory being shadowed to be an invariant set, such as an ECS or a heteroclinic connection. Indeed, one could select intervals of a turbulent trajectory that *approximately* transition between two known ECSs, utilize these as network edges, and detect the shadowing of these edges using the exact method proposed here. Doing so would circumvent the need to converge heteroclinic connections using computationally expensive numerical solvers, and likely still provide a reasonable network-like approximation of the chaotic set.

Moreover, while it is possible to relate important processes in turbulence to underlying ECS [74], it can be difficult. There are many instances in which one has knowledge of turbulence exhibiting a physical process—such as an extreme event [75]—but does not know of an underlying ECS that describes that process. Consider, instead, selecting a single snippet of turbulent flow at the onset of an extreme event. Any other interval of turbulent flow that shadows this snippet likely goes on to exhibit an extreme events itself; detecting the shadowing of this snippet provides an oppurtunity to forecast the extreme event and apply a control scheme to the flow, potentially inhibiting the extreme behavior altogether. Indeed, while ECS are useful objects due to their compactness and coordinate-free nature, exploring the shadowing of turbulent snippets is an important avenue of future research that could render a network-based description of the chaotic set much more practical to construct.

At this juncture, we return to the shadowing properties, Property **S1**-Property **S5**, discussed in Chapter 1.

As Figure 3.12 illustrates, turbulence can shadow multiple solutions at once, and these solutions can also shadow each other during this same interval (Property **S5**). While one could select whether RPO_3 or RPO_8 is shadowed "better" by comparing which has the smallest E_d, this has an implicit bias on the use of the L_2 norm to define E_d; a different norm could select a different "best" solution, rendering the notion of "best" ill-defined. At the moment, there is no coordinate-free measure with which to select which shadowing interval is best (Property **S4**). Indeed, for likely all definitions of norm, shadowing will occur at on a spectrum, at various degrees of quality (Property **S3**), as seen in Axiom A chaos. However, one may introduce a threshold of what is considered "sufficiently" shadowed—as we did here to enforce visual similarity—depending on the use case.

For the thresholds used here, shadowing is observed quite often, and over a variety of durations. While many shadowing events persisted longer than the ECS's period, the mean duration of shadowing is of order γ_n^{-1} (Property **S2**). Hence, we find that sub-period shadowing events occur. Intriguingly, had shadowing for an entire period been enforced, intervals of time describing the co-shadowing of orbits that are only similar for sub-intervals of there period, like those illustrated in Figure 3.12 and Figure 3.13(b), would have been missed.

Indeed, the only property not seen in turbulence is Property **S1**, which was known to be broken at the onset of this investigation. An important consequence of Property **S1** being broken is that the evolution of observables of the turbulent flow may not be very well captured during shadowing. For instance, in the example shown in Figure 3.1(a), both the energy and dissipation rate are found to differ rather substantially from those characterized by RPO_1, despite the flow fields appearing almost indistinguishable. When $d^\perp$ is infinitesimal, all smooth observables become well approximated during shadowing; as $d^\perp$ becomes large, so may the discrepancies in observables. Figure 3.1 suggests that visual similarity

is not a strict enough distance threshold to imply similarity in the evolution of observables like $\mathcal{E}$ and $\mathcal{D}$. Shadowing events of higher quality are required for a robust description of observable evolution through shadowing. Of course, if a specific physical observable, $a(\mathbf{u})$, is of interest, it may be possible to replace E_{vis} or E_d with an appropriately defined E_a. This would select for intervals of co-evolution in which there is agreement of the observable: $a(\mathbf{u}(t)) \approx a(\mathbf{u}_n(t))$ for all t in the interval.

In conclusion, we have constructed a very general method for quantifying shadowing in turbulence, one with applications to constructing a network-like model of the chaotic set, forecasting and control, as well as the prediction of turbulent observables. Although the collections of ECSs used in this study are rather sparse, turbulence shadows known solutions for a relatively large fraction of time (for instance, about %30 of the time in TCF(b)). A description of turbulence in terms of shadowing ECSs will only improve as more ECSs are identified. While identifying ECSs can be a computationally difficult task, we have also outlined an avenue for future work that would utilize shadowing to describe turbulent flow in terms of finitely long turbulent snippets, circumventing the need for computing ECS entirely. Just as periodic orbits were used to construct both a deterministic (through shadowing) and a statistical (through a Markov model) picture of Axiom A chaos, future work will also aim to formalize a statistical picture of turbulence from ECS. A great deal of work has been conducted to show that ECSs can form a backbone of the chaotic set of turbulence [70, 47, 48, 16, 56]. The work presented here provides a quantitative machinery for understanding how turbulence explores this backbone, opening the door for exciting new ways to explore reduced-order, network-like models of turbulence.

REFERENCES

[1] T. Yamada *et al.*, "Anatomy of plasma turbulence," *Nature Physics*, vol. 4, no. 9, pp. 721–725, Sep. 2008.

[2] L. Wang and H. Garnier, Eds., *System Identification, Environmental Modelling, and Control System Design*. London: Springer London, 2012, ISBN: 978-0-85729-973-4 978-0-85729-974-1.

[3] L. Herrmann, M. Granz, and T. Landgraf, "Chaotic dynamics are intrinsic to neural network training with SGD," in *Advances in Neural Information Processing Systems*, A. H. Oh, A. Agarwal, D. Belgrave, and K. Cho, Eds., 2022.

[4] E. N. Lorenz, "Deterministic Nonperiodic Flow," *Journal of the Atmospheric Sciences*, vol. 20, no. 2, pp. 130–141, Mar. 1963.

[5] G. Haller, B. Kaszás, A. Liu, and J. Axås. "Nonlinear Model Reduction to Fractional and Mixed-Mode Spectral Submanifolds." arXiv: 2305.15796 [nlin]. (May 25, 2023), (visited on 06/07/2023), preprint.

[6] V. Araújo and M. Viana, "Hyperbolic dynamical systems," in *Encyclopedia of Complexity and Systems Science*, R. A. Meyers, Ed., New York, NY: Springer New York, 2009, pp. 4723–4737, ISBN: 978-0-387-30440-3.

[7] J.-P. Eckmann and D. Ruelle, "Ergodic theory of chaos and strange attractors," *Reviews of Modern Physics*, vol. 57, no. 3, pp. 617–656, Jul. 1, 1985.

[8] R. L. Devaney, *An Introduction to Chaotic Dynamical Systems* (Studies in Nonlinearity), 2nd ed., paperback ed. Boulder, Colo: Westview Press, 2003, 335 pp., ISBN: 978-0-8133-4085-2.

[9] P. Cvitanović, R. artuso, G. Tanner, G. Vattay, and R. Manieri, *Chaos: Classical and Quantum*. Niels Bohr Inst., 2016.

[10] R. Bowen, "Markov Partitions for Axiom A Diffeomorphisms," *American Journal of Mathematics*, vol. 92, no. 3, p. 725, Jul. 1970. JSTOR: 2373370.

[11] P. Cvitanović, "Trace Formulas in Classical Dynamical Systems," in *Supersymmetry and Trace Formulae*, I. V. Lerner, J. P. Keating, and D. E. Khmelnitskii, Eds., vol. 370, Boston, MA: Springer US, 1999, pp. 85–102, ISBN: 978-1-4613-7212-7 978-1-4615-4875-1.

[12] P. Gaspard, *Chaos, Scattering and Statistical Mechanics* (Cambridge Nonlinear Science Series 9), New ed. Cambridge: Cambridge Univ. Press, 2005, 475 pp., ISBN: 978-0-521-01825-8.

[13] L. P. Kadanoff and C. Tang, "Escape from strange repellers," *Proceedings of the National Academy of Sciences*, vol. 81, p. 1276, 1984.

[14] D. V. Anosov and Y. G. Sinai, "Some Smooth Ergodic Systems," *Russian Mathematical Surveys*, vol. 22, no. 5, pp. 103–167, Oct. 31, 1967.

[15] S. M. Hammel, J. A. Yorke, and C. Grebogi, "Numerical orbits of chaotic processes represent true orbits," *Bulletin of the American Mathematical Society*, vol. 19, no. 2, pp. 465–469, 1988.

[16] M. C. Krygier, J. L. Pughe-Sanford, and R. O. Grigoriev, "Exact coherent structures and shadowing in turbulent Taylor–Couette flow," *Journal of Fluid Mechanics*, vol. 923, A7, Sep. 25, 2021.

[17] A. N. Kolmogorov, "The local structure of turbulence in incompressible viscous fluid for very large Reynolds numbers," *Cr Acad. Sci. URSS*, vol. 30, pp. 301–305, 1941.

[18] J. Nikuradse, *Gesetzmässigkeiten Der Turbulenten Strömung in Glatten Rohren: Aus d. Kaiser-wilhelm-institut Für Strömungsforschg, Göttingen* (Forschungsheft Auf d. Geb. d. Ingenieurwesens). VDI-Verlag, 1932.

[19] A. K. M. F. Hussain, "Coherent structures—reality and myth," *Physics of Fluids*, vol. 26, no. 10, p. 2816, 1983.

[20] S. Smale, "Differentiable dynamical systems," *Bulletin of the American Mathematical Society*, vol. 73, no. 6, pp. 747–817, 1967.

[21] D. W. Moore and E. A. Spiegel, "A Thermally Excited Non-Linear Oscillator," *The Astrophysical Journal*, vol. 143, p. 871, Mar. 1966.

[22] E. A. Spiegel, "Chaos: A mixed metaphor for turbulence," *Proceedings of the Royal Society of London. A. Mathematical and Physical Sciences*, vol. 413, no. 1844, pp. 87–95, Sep. 8, 1987.

[23] F. Christiansen, P. Cvitanovic, and V. Putkaradze, "Spatiotemporal chaos in terms of unstable recurrent patterns," *Nonlinearity*, vol. 10, no. 1, pp. 55–70, Jan. 1, 1997.

[24] D. Viswanath, "Recurrent motions within plane Couette turbulence," *Journal of Fluid Mechanics*, vol. 580, pp. 339–358, Jun. 10, 2007.

[25] T. Itano and S. C. Generalis, "Hairpin vortex solution in planar couette flow: A tapestry of knotted vortices," *Physical Review Letters*, vol. 102, no. 11, p. 114 501, Mar. 2009.

[26] P. Cvitanović and J. F. Gibson, "Geometry of the turbulence in wall-bounded shear flows: Periodic orbits," *Physica Scripta*, vol. T142, p. 014 007, Dec. 1, 2010.

[27] H. Poincaré, *Les Méthodes Nouvelles de La Mécanique Céleste*. Gauthier-Villars, 1899, vol. 3.

[28] L. van Veen and G. Kawahara, "Homoclinic tangle on the edge of shear turbulence," *Phys. Rev. Lett.*, vol. 107, p. 114 501, 11 Sep. 2011.

[29] B. Suri, R. K. Pallantla, M. F. Schatz, and R. O. Grigoriev, "Heteroclinic and homoclinic connections in a Kolmogorov-like flow," *Physical Review E*, vol. 100, no. 1, p. 013 112, Jul. 25, 2019.

[30] M. Nagata, "Three-dimensional finite-amplitude solutions in plane Couette flow: Bifurcation from infinity," *Journal of Fluid Mechanics*, vol. 217, pp. 519–527, Aug. 1990.

[31] R. M. Clever and F. H. Busse, "Tertiary and quaternary solutions for plane Couette flow," *Journal of Fluid Mechanics*, vol. 344, pp. 137–153, 1997.

[32] J. F. Gibson, J. Halcrow, and P. Cvitanović, "Visualizing the geometry of state space in plane Couette flow," *Journal of Fluid Mechanics*, vol. 611, pp. 107–130, Sep. 25, 2008.

[33] B. Suri, J. Tithof, R. O. Grigoriev, and M. F. Schatz, "Forecasting Fluid Flows Using the Geometry of Turbulence," *Physical Review Letters*, vol. 118, no. 11, p. 114 501, Mar. 15, 2017.

[34] B. Suri, J. Tithof, R. O. Grigoriev, and M. F. Schatz, "Unstable equilibria and invariant manifolds in quasi-two-dimensional Kolmogorov-like flow," *Physical Review E*, vol. 98, no. 2, p. 023 105, Aug. 13, 2018.

[35] H. Faisst and B. Eckhardt, "Traveling waves in pipe flow," *Physical Review Letters*, vol. 91, no. 22, p. 224 502, Nov. 2003.

[36] B. Hof *et al.*, "Experimental Observation of Nonlinear Traveling Waves in Turbulent Pipe Flow," *Science*, vol. 305, no. 5690, pp. 1594–1598, Sep. 10, 2004.

[37] A. de Lozar, F. Mellibovsky, M. Avila, and B. Hof, "Edge State in Pipe Flow Experiments," *Physical Review Letters*, vol. 108, no. 21, p. 214 502, May 21, 2012.

[38] G. Lemoult, K. Gumowski, J.-L. Aider, and J. E. Wesfreid, "Turbulent spots in channel flow: An experimental study," *The European Physical Journal E*, vol. 37, no. 4, p. 25, 2014.

[39] J. S. Park and M. D. Graham, "Exact coherent states and connections to turbulent dynamics in minimal channel flow," *Journal of Fluid Mechanics*, vol. 782, pp. 430–454, Nov. 10, 2015.

[40] F. Mellibovsky, A. Meseguer, T. M. Schneider, and B. Eckhardt, "Transition in localized pipe flow turbulence," *Physical Review Letters*, vol. 103, no. 5, p. 054 502, 2009.

[41] R. R. Kerswell and O. R. Tutty, "Recurrence of travelling waves in transitional pipe flow," *Journal of Fluid Mechanics*, vol. 584, pp. 69–102, Aug. 10, 2007.

[42] B. Eckhardt and S. Zammert, "Small scale exact coherent structures at large Reynolds numbers in plane Couette flow," *Nonlinearity*, vol. 31, no. 2, R66, 2018.

[43] G. Kawahara and S. Kida, "Periodic motion embedded in plane Couette turbulence: Regeneration cycle and burst," *Journal of Fluid Mechanics*, vol. 449, pp. 291–300, Dec. 25, 2001.

[44] G. J. Chandler and R. R. Kerswell, "Invariant recurrent solutions embedded in a turbulent two-dimensional Kolmogorov flow," *Journal of Fluid Mechanics*, vol. 722, pp. 554–595, May 10, 2013.

[45] B. Suri, L. Kageorge, R. O. Grigoriev, and M. F. Schatz, "Capturing Turbulent Dynamics and Statistics in Experiments with Unstable Periodic Orbits," *Physical Review Letters*, vol. 125, no. 6, p. 064 501, Aug. 5, 2020.

[46] J. M. Lopez and F. Marques, "Dynamics of Three-Tori in a Periodically Forced Navier-Stokes Flow," *Physical Review Letters*, vol. 85, no. 5, pp. 972–975, Jul. 31, 2000.

[47] N. B. Budanur, K. Y. Short, M. Farazmand, A. P. Willis, and P. Cvitanović, "Relative periodic orbits form the backbone of turbulent pipe flow," *Journal of Fluid Mechanics*, vol. 833, pp. 274–301, Dec. 25, 2017.

[48] G. Yalnız, B. Hof, and N. B. Budanur, "Coarse Graining the State Space of a Turbulent Flow Using Periodic Orbits," *Physical Review Letters*, vol. 126, no. 24, p. 244 502, Jun. 16, 2021.

[49] T. M. Schneider, B. Eckhardt, and J. Vollmer, "Statistical analysis of coherent structures in transitional pipe flow," *Physical Review E*, vol. 75, no. 6, p. 066 313, Jun. 26, 2007.

[50] C. C. Maiocchi, V. Lucarini, and A. Gritsun, "Decomposing the dynamics of the Lorenz 1963 model using unstable periodic orbits: Averages, transitions, and quasi-invariant sets," *Chaos: An Interdisciplinary Journal of Nonlinear Science*, vol. 32, no. 3, p. 033 129, Mar. 2022.

[51] C. C. Maiocchi, V. Lucarini, A. Gritsun, and Y. Sato, "Heterogeneity of the Attractor of the Lorenz '96 Model: Lyapunov Analysis, Unstable Periodic Orbits, and Shadowing Properties," version 1, 2023.

[52] A. N. Souza, "Transforming Butterflies into Graphs: Statistics of Chaotic and Turbulent Systems," version 1, 2023.

[53] D. Fernex, B. R. Noack, and R. Semaan, "Cluster-based network modeling—From snapshots to complex dynamical systems," *Science Advances*, vol. 7, no. 25, eabf5006, Jun. 18, 2021.

[54] J. Page and R. R. Kerswell, "Searching turbulence for periodic orbits with dynamic mode decomposition," *Journal of Fluid Mechanics*, vol. 886, A28, Mar. 10, 2020.

[55] J. L. Pughe-Sanford, S. Quinn, L. Balabanski, and R. O. Grigoriev, "Computing Chaotic Time-Averages from a Small Number of Periodic Orbits," *(submitted)*, 2023.

[56] C. J. Crowley, J. L. Pughe-Sanford, W. Toler, M. C. Krygier, R. O. Grigoriev, and M. F. Schatz, "Turbulence tracks recurrent solutions," *Proceedings of the National Academy of Sciences*, vol. 119, no. 34, e2120665119, Aug. 23, 2022.

[57] C. J. Crowley, J. L. Pughe-Sanford, W. Toler, R. O. Grigoriev, and M. F. Schatz, "Observing a dynamical skeleton of turbulence in Taylor–Couette flow experiments," *Philosophical Transactions of the Royal Society A: Mathematical, Physical and Engineering Sciences*, vol. 381, no. 2243, p. 20 220 137, Mar. 20, 2023.

[58] M. C. Krygier, "Exact Coherent Structures in turbulent small-aspect-ratio Taylor-Couette flow," Ph.D. dissertation, Georgia Institute of Technology, Atlanta, GA, 2019.

[59] C. J. Crowley, "A Dissertation Presented to The Academic Faculty," Georgia Institute of Technology, 2022.

[60] M. Avila, M. Grimes, J. M. Lopez, and F. Marques, "Global endwall effects on centrifugally stable flows," *Physics of Fluids*, vol. 20, no. 10, p. 104 104, Oct. 2008.

[61] I. Mercader, O. Batiste, and A. Alonso, "An efficient spectral code for incompressible flows in cylindrical geometries," *Computers & Fluids*, vol. 39, no. 2, pp. 215–224, Feb. 2010.

[62] M. Avila, "Stability and Angular-Momentum Transport of Fluid Flows between Corotating Cylinders," *Physical Review Letters*, vol. 108, no. 12, p. 124 501, Mar. 19, 2012.

[63] S. Hugues and A. Randriamampianina, "An improved projection scheme applied to pseudospectral methods for the incompressible Navier-Stokes equations," *International Journal for Numerical Methods in Fluids*, vol. 28, no. 3, pp. 501–521, Sep. 15, 1998.

[64] S. A. Orszag and A. T. Patera, "Secondary instability of wall-bounded shear flows," *Journal of Fluid Mechanics*, vol. 128, p. 347, -1 Mar. 1983.

[65] E. L. Allgower and K. Georg, *Introduction to Numerical Continuation Methods*. Society for Industrial and Applied Mathematics, Jan. 2003, ISBN: 978-0-89871-544-6 978-0-89871-915-4.

[66] K. Hochstrate, J. Abshagen, M. Avila, C. Will, and G. Pfister, "Decay of turbulent bursting in enclosed flows," in *Seventh IUTAM Symposium on Laminar-Turbulent Transition*, P. Schlatter and D. S. Henningson, Eds., vol. 18, Dordrecht: Springer Netherlands, 2010, pp. 195–200, ISBN: 978-90-481-3722-0 978-90-481-3723-7.

[67] T. Hastie, R. Tibshirani, and J. H. Friedman, *The Elements of Statistical Learning: Data Mining, Inference, and Prediction* (Springer Series in Statistics), 2nd ed. New York, NY: Springer, 2009, 745 pp., ISBN: 978-0-387-84857-0 978-0-387-84858-7.

[68] B. Fiedler, B. Sandstede, A. Scheel, and C. Wulff, "Bifurcation from relative equilibria of noncompact group actions: Skew products, meanders, and drifts," *Documenta Mathematica*, vol. 1, pp. 479–505, 1996.

[69] B. Sandstede, A. Scheel, and C. Wulff, "Dynamical behavior of patterns with Euclidean symmetry," in *Pattern Formation in Continuous and Coupled Systems*, New York: Springer, 1999, pp. 249–264.

[70] P. Cvitanović, "Recurrent flows: The clockwork behind turbulence," *Journal of Fluid Mechanics*, vol. 726, pp. 1–4, Jul. 10, 2013.

[71] G. Yalnız and N. B. Budanur, "Inferring symbolic dynamics of chaotic flows from persistence," *Chaos: An Interdisciplinary Journal of Nonlinear Science*, vol. 30, no. 3, p. 033 109, Mar. 2020.

[72] C.-A. Yeh, M. Gopalakrishnan Meena, and K. Taira, "Network broadcast analysis and control of turbulent flows," *Journal of Fluid Mechanics*, vol. 910, A15, Mar. 10, 2021.

[73] O. Ashtari and T. M. Schneider, "Jacobian-free variational method for constructing connecting orbits in nonlinear dynamical systems," *arXiv preprint arXiv:2301.11704*, 2023.

[74] F. Waleffe, "Three-Dimensional Coherent States in Plane Shear Flows," *Physical Review Letters*, vol. 81, no. 19, pp. 4140–4143, Nov. 9, 1998.

[75] M. Farazmand and T. P. Sapsis, "A variational approach to probing extreme events in turbulent dynamical systems," *Science Advances*, vol. 3, no. 9, e1701533, Sep. 2017.

VITA

Joshua Pughe-Sanford was born on March 10, 1995 in Bridgewater, NJ to parents Roberta Pughe and Robert Sanford and brother Zachary Pughe-Sanford. His family has grown quite a lot since then. He attended Emory University in 2013, where he received his Bachelor of Science in Physics, and started graduate school at Georgia Tech in 2017, where he joined the Center for Non-Linear Science working with Dr. Roman Grigoriev. Graduating in 2023, he and his cats, Pickle and Bean, are off to explore the world.